Pion-less effective field theory for atomic nuclei and lattice nuclei

Pion-less effective field theory for atomic nuclei and lattice nuclei

A. Bansal,[1] S. Binder,[1,2] A. Ekström,[3,2] G. Hagen,[2,1] G. R. Jansen,[4,2] and T. Papenbrock[1,2]
[1]*Department of Physics and Astronomy, University of Tennessee, Knoxville, Tennessee 37996, USA*
[2]*Physics Division, Oak Ridge National Laboratory, Oak Ridge, Tennessee 37831, USA*
[3]*Department of Physics, Chalmers University of Technology, SE-412 96 Göteborg, Sweden*
[4]*National Center for Computational Sciences, Oak Ridge National Laboratory, Oak Ridge, Tennessee 37831, USA*

(Received 29 December 2017; revised manuscript received 29 June 2018; published 1 November 2018)

We compute the medium-mass nuclei ^{16}O and ^{40}Ca using pion-less effective field theory (EFT) at next-to-leading order (NLO). The low-energy coefficients of the EFT Hamiltonian are adjusted to experimental data for nuclei with mass numbers $A = 2$ and 3, or alternatively to results from lattice quantum chromodynamics at an unphysical pion mass of 806 MeV. The EFT is implemented through a discrete variable representation in the harmonic oscillator basis. This approach ensures rapid convergence with respect to the size of the model space and facilitates the computation of medium-mass nuclei. At NLO the nuclei ^{16}O and ^{40}Ca are bound with respect to decay into alpha particles. Binding energies per nucleon are 9–10 MeV and 21–40 MeV at pion masses of 140 and 806 MeV, respectively.

DOI: 10.1103/PhysRevC.98.054301

I. INTRODUCTION

Pion-less effective field theory (EFT) is widely employed to describe the structure and reactions of the lightest nuclei [1–4]. Variants of this EFT have also been applied to describe halo nuclei [5–8] and dilute Fermi gases [9]. Lattice nuclei, i.e., nuclei computed from lattice quantum chromodynamics (QCD) [10], can also be described in pion-less EFT [11,12]. In that approach, the relevant low-energy coefficients (LECs) of the EFT are adjusted to data of light nuclei computed with lattice QCD, and predictions are made for heavier nuclei. Although present-day lattice QCD calculations of nuclei use unphysically large pion masses, one might expect that advances in that field will eventually allow us to tie nuclear structure to QCD.

^{16}O is the heaviest nucleus computed in pion-less EFT so far, and it was found to be unstable against break up into four ^{4}He nuclei at leading order (LO) [12]. We are aware of only a few applications of pion-less EFT to nuclear structure calculations beyond mass number $A \geqslant 4$: Platter *et al.* [13] found that no four-nucleon force is needed to describe ^{4}He at LO. This result was confirmed at next-to-leading order (NLO) by Kirscher *et al.* [14]; studies of heavier helium isotopes are presented in Refs. [15,16]. Very recently, Lensky *et al.* [17] studied ^{3,4}He at next-to-next-to-leading order. Stetcu *et al.* [18] computed ^{6}Li at LO and found it to be less bound than ^{4}He.

In contrast to pion-less EFT, chiral EFT [19–21] has been used to compute heavy nuclei up to the mass number $A = 100$ region [22–28]. We can only speculate about this discrepancy between chiral and pion-less EFTs. On one hand, it might be a concern that pion-less EFT—with a breakdown scale around the pion mass $m_\pi \approx 140$ MeV–cannot be used to describe heavy nuclei with Fermi momentum $k_F \approx 270$ MeV. On the other hand, the pion is still very massive compared to the Fermi energy of about 40 MeV. We also note that there could be a mismatch in infrastructure. Many of the powerful nuclear quantum many-body solvers [24,26,29–31] start from interactions in the harmonic oscillator basis, and matrix elements for interactions from chiral EFT [32–36] are readily available in this basis. No similar and well established infrastructure seems to exist for pion-less EFT.

This paper has two goals. First, we want to study heavier nuclei such as ^{16}O and ^{40}Ca with pion-less EFT. We will adjust the LECs of the EFT to both experimental data of light nuclei and to data from lattice QCD. Second, we want to formulate pion-less EFT directly in the harmonic oscillator basis. This project was started by Stetcu *et al.* [18] (with several applications to harmonically trapped systems [37–39]), and a formulation involving energy-dependent potentials is pursued by Haxton and co-workers [40–42]. Recently, Binder *et al.* [43] and Yang [44] used the J-matrix approach [45,46] to directly construct EFT potentials in the oscillator basis. Here, we follow and extend the work of Ref. [43] and formulate pion-less EFT as a discrete variable representation (DVR) [47–50]. A hallmark of the present work is that the finite oscillator space itself becomes the regulator, and no external regulator functions are employed. Similar to nuclear lattice EFT [51], this implementation tailors the EFT to the employed basis and thereby facilitates the computations of Hamiltonian matrix elements and nuclei.

Unfortunately, the computation of light nuclei in lattice QCD is not without controversy, and there is no consensus whether nuclear binding increases or decreases with increasing pion mass. The calculations in Refs. [10,52–54] infer bound-state energies from plateaus in the time propagation and find that nuclear binding increases with increasing pion mass. In contrast, the calculations in Refs. [55–57] construct

a potential from a Bethe-Salpeter wave function and find that lattice nuclei (computed at unphysically large pion masses) are less bound than real nuclei [58]. Both approaches have been used as input for the computation of increasingly heavier nuclei [12,59]. In this work, we follow Refs. [11,12] and use the lattice QCD results of Ref. [10] as input to constrain the LECs of our EFT. Similar lattice QCD results, which support an increase in binding energy with increasing pion mass, were also found by the other collaborations in Refs. [60,61].

This paper is organized as follows. In Sec. II we tailor pion-less EFT interactions to the harmonic oscillator basis using a DVR. In Sec. III we discuss the fitting procedure used to constrain LECs to data and lattice data, and present results for $A = 3, 4$ nuclei for a range of ultraviolet (UV) cutoffs. We use the NLO interactions to compute atomic and lattice ^{16}O and ^{40}Ca nuclei in Sec. IV. A summary of this paper is given in Sec. V. The formulation of the EFT in the harmonic oscillator basis involves several technical elements and many checks. For the purpose of readability this information is presented in a number of Appendixes.

II. PION-LESS EFFECTIVE FIELD THEORY IN THE OSCILLATOR BASIS

A. Pion-less EFT

We briefly introduce pion-less EFT and refer the reader to the reviews [1,62,63] for details on this extensive subject. In pion-less EFT, neutrons and protons are the relevant degrees of freedom, and the breakdown scale is given by the pion mass. Using naive dimensional analysis, nucleon-nucleon (NN) interactions in momentum space are

$$\begin{aligned} V_{NN}^{(0)}(\vec{p}', \vec{p}) &= C_S + C_T \vec{\sigma}_1 \cdot \vec{\sigma}_2, \\ V_{NN}^{(2)}(\vec{p}', \vec{p}) &= C_1 q^2 + C_2 k^2 + (C_3 q^2 + C_4 k^2) \vec{\sigma}_1 \cdot \vec{\sigma}_2 \\ &\quad - i C_5 \frac{\vec{\sigma}_1 + \vec{\sigma}_2}{2} \cdot (\vec{q} \times \vec{k}) \\ &\quad + C_6 (\vec{\sigma}_1 \cdot \vec{q})(\vec{\sigma}_2 \cdot \vec{q}) \\ &\quad + C_7 (\vec{\sigma}_1 \cdot \vec{k})(\vec{\sigma}_2 \cdot \vec{k}). \end{aligned} \tag{1}$$

Here $\vec{p}'$ and $\vec{p}$ are the outgoing and incoming relative momenta, respectively, and we use the shorthand $\vec{q} = \vec{p} - \vec{p}'$, $\vec{k} = (\vec{p}' + \vec{p})/2$ for the momentum transfer and the average momentum, respectively. The LECs are denoted as C_i, and the superscripts (0) and (2) on the potential denote the powers of the momenta.

The large scattering lengths in the singlet and triplet S waves, due to a weakly bound deuteron and almost bound dineutron, reflect the existence of another small momentum scale denoted by $\aleph \approx 40$ MeV, and lead to a modified power counting. In the singlet and triplet S partial waves the LO LECs are proportional to the respective scattering lengths, i.e., they scale as $1/\aleph$ instead of $1/m_\pi$, which was expected otherwise as the pion mass sets the breakdown scale. The unnatural size of both S-wave LECs (with respect to the expected scaling $1/m_\pi$) causes enhancement of their next higher-order correction relative to other terms in Eq. (1). Moreover, the S-wave LO potential is counted as $\mathcal{O}(Q^{-1})$, the enhanced higher-order S-wave correction then becomes of $\mathcal{O}(Q^0)$, and other NLO terms from naive counting enter only at $\mathcal{O}(Q^1)$ or higher; see Refs. [1,64,65] for details. Therefore, NLO pion-less EFT involves only S waves with the LO potentials,

$$\begin{aligned} V_{NN}^{\mathrm{LO}}(^1S_0) &= \tilde{C}_{^1S_0} = C_S - 3C_T, \\ V_{NN}^{\mathrm{LO}}(^3S_1) &= \tilde{C}_{^3S_1} = C_S + C_T, \end{aligned}$$

and the NLO potentials,

$$\begin{aligned} V_{NN}^{\mathrm{NLO}}(^1S_0) &= C_{^1S_0}(p^2 + p'^2), \\ V_{NN}^{\mathrm{NLO}}(^3S_1) &= C_{^3S_1}(p^2 + p'^2). \end{aligned} \tag{2}$$

Pion-less EFT can be used to reproduce the deuteron binding energy and the effective range expansion for low-energy NN scattering

$$k \cot \delta_0(k) = -\frac{1}{a_0} + \frac{1}{2} r_0 k^2 + \cdots . \tag{3}$$

This defines the S-wave scattering length a_0 and effective range r_0. Pion-less EFT yields the scattering length at LO, and the effective range at NLO.

To renormalize the three-nucleon system, the three-nucleon force (NNN) is promoted to LO [66]. There are many equivalent ways to write this contact [19,67], and we use

$$V_{NNN} = \frac{c_E}{F_\pi^4 \Lambda_\chi} \sum_{j \neq i} \vec{\tau}_i \cdot \vec{\tau}_j .$$

Here $\Lambda_\chi = 700$ MeV and $F_\pi = 92.4$ MeV are constants (employed in chiral EFT) that make c_E dimensionless; we include these for convenience only. Summarizing, the complete LO interaction is given by

$$V_{\mathrm{LO}} = V_{NN}^{\mathrm{LO}}(^1S_0) + V_{NN}^{\mathrm{LO}}(^3S_1) + V_{NNN}. \tag{4}$$

Our NLO potential consists of the terms (2) added to the LO potential Eq. (4). We note that no higher-rank nuclear many-body force enters at NLO in pion-less EFT [16,66,68,69]. We include the Coulomb interaction nonperturbatively at the level of single photon exchange, i.e., α_{em}/r. Here, α_{em} is the fine structure constant. We note that further electromagnetic corrections [70,71] enter up to NLO. We omit any such corrections in this work.

We will solve the NLO potential with a nonperturbative method, as done previously, for instance, in Refs. [14,17]. The reason is as follows. Nuclei heavier than ^{4}He computed with LO pion-less EFT potentials have been found to be unstable with respect to α-particle emission. Examples in this case are the nuclei ^{6}Li [18] and ^{16}O [12], and we found similar results for ^{16}O and ^{40}Ca. Thus the ground states of LO pion-less EFT potentials are clusters (probably gases of α particles, deuterons, and nucleons), but not self-bound nuclei. While the perturbative treatment of NLO terms could lead to energies that would mimic self-bound systems it cannot change the extended continuum wave function of a gaseous state into a bound-state wave function (which decays exponentially in position space and is localized). Thus we see it as mandatory to include the NLO terms of the potentials nonperturbatively. The application of a nonperturbative method might be valid only for UV cutoffs that are not too large, and we will limit

the range of cutoffs to up to about 700 MeV. Larger cutoffs are discussed in Appendix E in connection with the Wigner bound. For a perturbative treatment of the three-nucleon systems, we refer the reader to Ref. [4].

In this work, we compute nuclei such as ^{16}O and ^{40}Ca. This requires us to be judicious about the basis we want to employ. Very recently, Binder *et al.* [43] showed that EFTs can be formulated in the harmonic oscillator basis, and they performed converged calculations for heavy nuclei based on *NN* interactions alone. In what follows, we briefly review the essential ingredients of this approach.

B. Discrete variable representations

A finite harmonic oscillator basis imposes infrared (IR) and UV cutoffs [18,72–75]. These correspond to hard-wall boundary conditions in position and momentum space, respectively. They depend on the maximum number of oscillator quanta N included in the basis and on the oscillator length

$$b \equiv \sqrt{\hbar/(\mu\omega)}. \tag{5}$$

Here, μ is the reduced mass for the two-nucleon system, and $\hbar\omega$ is the oscillator spacing. In position space, the effective hard wall is located at the radius [76]

$$L = \sqrt{2(N+3/2+2)}b, \tag{6}$$

while in momentum space the radius Λ defining the UV cutoff is given by [77]

$$\Lambda = \sqrt{2(N+3/2+2)}\hbar/b. \tag{7}$$

For many-body systems, similar expressions were derived in Refs. [78,79]. The effective hard wall in position space modifies the asymptotic tail of bound-state wave functions and introduces—akin to the Lüscher [80] formula—a correction to bound-state energies and other observables [75,81,82].

We will formulate pion-less EFT in a spherical harmonic oscillator basis. The radial basis functions at orbital angular momentum l are

$$\psi_{n,l}(r) = (-1)^n \sqrt{\frac{2n!}{\Gamma(n+l+3/2)b^3}} \left(\frac{r}{b}\right)^l \times e^{-(1/2)(r^2/b^2)} L_n^{l+(1/2)}\left(\frac{r^2}{b^2}\right) \tag{8}$$

in position space, and

$$\tilde{\psi}_{n,l}(k) = \sqrt{\frac{2n!b^3}{\Gamma(n+l+3/2)}}(kb)^l e^{-(1/2)k^2b^2} L_n^{l+(1/2)}(k^2b^2) \tag{9}$$

in momentum space. Here, $L_n^{l+1/2}$ denotes the generalized Laguerre polynomial. The finite basis consists of all states with $2n+l \leqslant N$. At fixed l, we employ the shorthand

$$N_l \equiv (N-l)/2 \tag{10}$$

for the maximum radial quantum number.

For EFT applications in a finite harmonic oscillator basis it is useful to replace the oscillator basis functions by the eigenfunctions $\phi_{\mu,l}(k)$ of the squared momentum operator.

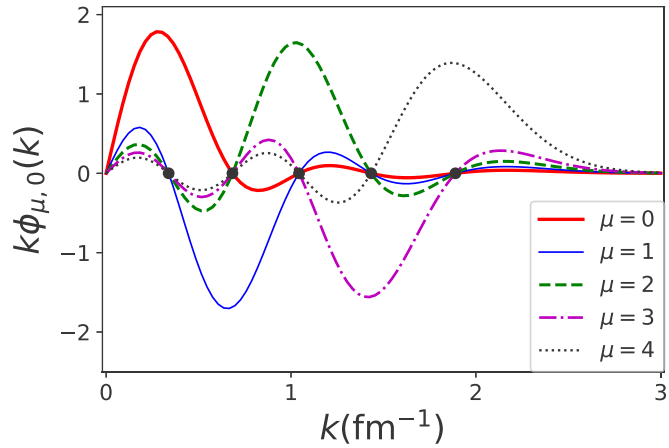

FIG. 1. The S wave eigenfunctions $\phi_{\mu,0}(k)$ of the squared momentum operator [plotted as $k\phi_{\mu,0}(k)$] for $\mu = 0, 1, \ldots N_0$) corresponding to discrete momentum eigenvalues, shown as a function of momentum for a finite harmonic oscillator basis with $N = 8$, $\hbar\omega = 22$ MeV. The solid black dots on the x axis indicate the discrete momentum eigenvalues.

Figure 1 shows the S-wave the eigenfunctions $\phi_{\mu,0}(k)$ operator with $\mu = 0, 1 \ldots, N_0$ for the oscillator model space $N = 8$, $\hbar\omega = 22$ MeV. The discrete momentum eigenvalues $k_{\mu,l}$, shown as dots in Fig. 1, fulfill

$$L_{N_l+1}^{l+1/2}(k_{\mu,l}^2 b^2) = 0. \tag{11}$$

We see that the corresponding eigenfunctions are localized around their eigenvalues and zero at other eigenvalues, thus forming a DVR, i.e., a discrete mesh that provides us with a basis in Hilbert space. For a detailed description of DVRs we refer the reader to some of the original works in quantum chemistry [47–49] and nuclear physics [50], and to the reviews [83,84]. In the present paper, we follow the notation of Ref. [43] and briefly summarize a few relevant results.

The eigenfunctions $\phi_{\mu,l}(k)$ can be expressed as

$$\tilde{\phi}_{\mu,l}(k) = \langle k, l|\phi_{\mu,l}\rangle = \frac{k_{\mu,l}/b}{k_{\mu,l}^2 - k^2}\tilde{\psi}_{N_l+1,l}(k). \tag{12}$$

This expression, when taken together with $\tilde{\psi}_{N_l+1,l}(k_{\mu,l}) = 0$ [implied by Eq. (11)] illustrates the key DVR property,

$$\tilde{\phi}_{\nu,l}(k_{\mu,l}) = \delta_\nu^\mu c_{\nu,l}^{-1}. \tag{13}$$

Here,

$$c_{\mu,l} \equiv \frac{k_{\mu,l}b}{\sqrt{(N_l+1)(N_l+l+3/2)}\tilde{\psi}_{N_l,l}(k_{\mu,l})} \tag{14}$$

is a normalization constant.

There are many ways to express the DVR wave functions. The expression

$$\tilde{\phi}_{\mu,l}(k) = c_{\mu,l}\sum_{n=0}^{N_l}\tilde{\psi}_{n,l}(k_{\mu,l})\tilde{\psi}_{n,l}(k) \tag{15}$$

is useful, because it exhibits the expansion in terms of the harmonic oscillator basis functions. In general, DVRs facilitate the computation of matrix elements (as quadratures

are replaced by sums over grid points). When formulated in momentum space, they are a most natural implementation of an EFT outside the plane-wave basis. In Appendix B we consider other DVRs in the oscillator basis that are based on a different set of discrete momentum points.

Due to localized nature of a DVR, the scalar product of functions $f(k)$ and $g(k)$ with angular momentum l can be defined as sum over the discrete eigenstates, i.e.,

$$\langle f|g\rangle_{\rm DVR} \equiv \sum_{\mu=0}^{N_l} c_{\mu,l}^2 f^*(k_{\mu,l}) g(k_{\mu,l}). \tag{16}$$

In our case, this overlap results from employing (N_l+1)-point Gauss-Laguerre quadrature in the computation of the exact scalar product,

$$\langle f|g\rangle \equiv \int_0^\infty dk k^2 f^*(k) g(k). \tag{17}$$

Thus, $\langle f|g\rangle_{\rm DVR} = \langle f|g\rangle$ for functions f and g that are spanned by the finite harmonic oscillator space. In other cases, the scalar product in Eq. (16) is an approximation of Eq. (17) [43]. We note that this approximation is consistent with EFT ideas as it neglects high-momentum contributions. In this paper, we will frequently evaluate matrix elements of operators in the DVR. In such cases, the subscript DVR will appear on the operator. As we will see, the DVR yields simple expressions for matrix elements of interactions and currents from EFT because the latter are usually expressed in momentum space.

The DVR basis states $|\phi_{\mu,l}\rangle$ are related to the wave functions (8) and (9) via the definitions

$$\phi_{\mu,l}(r) \equiv \langle r,l|\phi_{\mu,l}\rangle, \quad \tilde\phi_{\mu,l}(k) \equiv \langle k,l|\phi_{\mu,l}\rangle. \tag{18}$$

Given the momentum-space matrix element $V(k',l';k,l) \equiv \langle k',l'|\hat V|k,l\rangle$ in the partial-wave basis, we have in the DVR,

$$\langle \phi_{\nu,l'}|\hat V_{\rm DVR}|\phi_{\mu,l}\rangle = c_{\nu,l'} c_{\mu,l} V(k_{\nu,l'},l';k_{\mu,l},l). \tag{19}$$

Thus, the computation of matrix elements is very convenient in the DVR basis (as it is merely a function call) once the EFT interaction is available in the partial wave basis. We also note that the momentum space matrix elements of the DVR interaction $\langle k',l'|V_{\rm DVR}|k,l\rangle$ agree with the original interaction $V(k',l';k,l)$ at the DVR momentum points $(k',k) = (k_{\mu,l'},k_{\nu,l})$ with $\nu = 0,\dots N_{l'}$ and $\mu = 0,\dots N_l$. One can therefore ask to what extent does the resulting interaction, i.e., the left-hand side of Eq. (19), preserve the low-momentum or IR properties of $V(k',l';k,l)$? To explore this question we express the momentum space matrix elements of the DVR interaction as

$$\begin{aligned}
&\langle k',l'|V_{\rm DVR}|k,l\rangle \\
&\quad = \sum_{\mu=0}^{N_l}\sum_{\nu=0}^{N_{l'}} \langle \phi_{\nu,l'}|\hat V_{\rm DVR}|\phi_{\mu,l}\rangle \tilde\phi_{\nu,l'}(k')\tilde\phi_{\mu,l}(k) \\
&\quad = \sum_{\mu=0}^{N_l}\sum_{\nu=0}^{N_{l'}} c_{\mu,l}c_{\nu,l'}\tilde\phi_{\nu,l'}(k')\tilde\phi_{\mu,l}(k) V(k'_\nu,l';k_\mu,l).
\end{aligned} \tag{20}$$

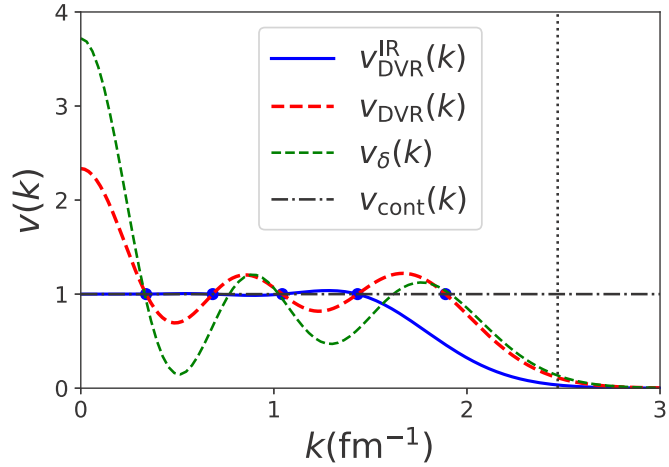

FIG. 2. The dashed red (solid blue) curve shows the contact interaction in the DVR basis (with IR improvement) to be compared with the original momentum-space interaction $v(k) = 1$ shown as a dash-dotted black line. The thin green dashed curve shows the contact (i.e., a δ function) in a finite harmonic oscillator basis with $N = 8$, $\hbar\omega = 22$ MeV, $l = 0$ for reference. The solid blue dots represent the DVR momenta. The dotted black line marks the location of the UV cutoff introduced by the finite oscillator basis.

This shows that the low-momentum expression of the left-hand side is a superposition of matrix elements. Though the IR cutoff of the basis is $k_{0,l}$ at angular momentum l, the interaction does not vanish for $k, k' < k_{0,l}$. In what follows, we will therefore improve its IR behavior. Although the contribution from the interactions at low momentum are reduced by the integration measure dkk^2 when it acts on wave functions, the incorrect IR behavior raises questions regarding the effective-range expansion of the DVR potential.

C. IR improvement of the *NN* interaction

Let us consider the case of a *NN* contact,

$$V(k',l'=0;k,l=0) = C_{\rm LO}, \tag{21}$$

where $C_{\rm LO}$ is the coupling strength. The corresponding DVR interaction is

$$\langle k',0|V^{\rm IR}_{\rm DVR}|k,0\rangle = C_{\rm LO} v_{\rm DVR}(k') v_{\rm DVR}(k) \tag{22}$$

with

$$v_{\rm DVR}(k) \equiv \sum_{\mu=0}^{N_0} c_{\mu,0}\tilde\phi_{\mu,0}(k). \tag{23}$$

Clearly, the DVR interaction differs from the original potential (21), which we now rewrite as $C_{\rm LO}v(k)v(k')$ with $v(k) = 1$. Figure 2 shows $v(k) = 1$ as the horizontal dash-dotted line, and the DVR result $v_{\rm DVR}$ as the dashed red line. The discrete DVR momenta are shown as solid dots. We see that $v_{\rm DVR}$ coincides with the original $v(k)$ only at these momenta, as expected for a DVR. The δ function, evaluated exactly in the oscillator basis, is shown as v_δ. It exhibits the strongest oscillations (and particularly large deviations at small momenta) from $v(k) = 1$. The vertical dotted line indicates the

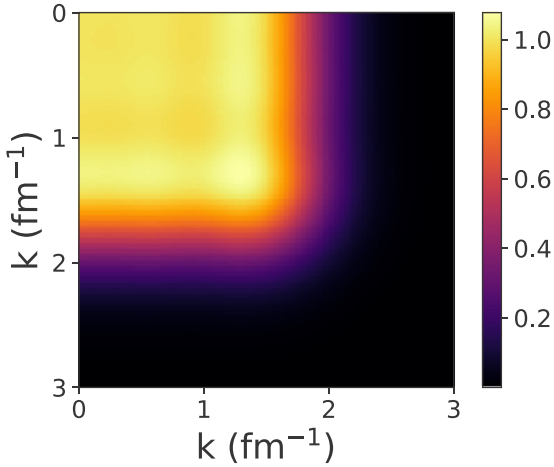

FIG. 3. The IR improved DVR contact interaction $V^{\rm IR}_{\rm DVR}$ plotted in momentum space. The axes represent momentum in units of fm^{-1}.

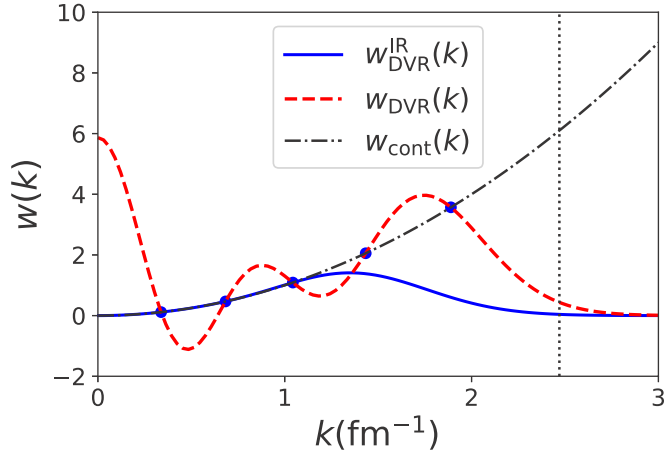

FIG. 4. The solid blue (dashed red) curve shows the NLO interaction term tailored to finite harmonic oscillator basis through DVR with (without) IR improvement. The solid blue dots represent discrete momentum eigenvalues in the model space $N = 8$, $\hbar\omega = 22$ MeV, and $l = 0$. The dotted black line depicts sharp cutoff Λ introduced by finite harmonic oscillator basis and the dash-dotted black line plots the interaction in continuous momentum basis.

UV cutoff in Eq. (7); as expected $v_{\rm DVR}$ rapidly vanishes here. Regarding the IR properties of the DVR interaction, we find that $v(k)$ and $v_{\rm DVR}(k)$ are indeed very different at lowest momenta. This is not unexpected: The finite oscillator basis introduces an IR cutoff (set by the smallest discrete momentum), and thus one has no control for small momenta. We will correct this in what follows.

To improve the IR behavior, we return to Eq. (23). This function is a superposition of functions $\tilde\phi_{\mu,0}(k)$ localized around $k \approx k_{\mu,0}$, and with weights $c_{\mu,0}$. The key idea is to force this function to have the value 1 at $k = 0$ by altering the weight $c_{N_0,0}$ of the highest-momentum DVR function $\tilde\phi_{N_0,0}(k)$. This is in the EFT spirit, because we improve the accuracy at low momentum at the cost of possible loss of accuracy at high momentum. Thus, we define new coefficients

$$\bar c_{\mu,0} \equiv c_{\mu,0}, \quad \text{for } \mu = 0,\dots,N_0-1,$$
$$\bar c_{N_0,0} \equiv \left(1 - \sum_{\nu=0}^{N_0-1} \tilde\phi_{\nu,l}(0) c_{\nu,0}\right) \Big/ \tilde\phi_{N_0,0}(0) \qquad (24)$$

and consider the IR improved DVR potential

$$v^{\rm IR}_{\rm DVR}(k) = C_{\rm LO} \sum_{\mu=0}^{N_0} \bar c_{\mu,0} \tilde\phi_{\mu,0}(k). \qquad (25)$$

By construction, it fulfills $v^{\rm IR}_{\rm DVR}(k) = 1$ for discrete momenta $k \in \{0, k_{0,0}, \dots, k_{N_0-1,0}\}$. The IR improved contact is shown as the solid blue line in Fig. 2. The IR improvement at $k = 0$ is obvious, and the oscillations are reduced substantially. In Appendix C we show that the curvature of $v^{\rm IR}_{\rm DVR}(k)$ at $k = 0$ decreases as N^{-1} as the basis size is increased. Thus, effective range corrections are suppressed, as expected from a proper EFT. Summarizing, the IR improved DVR contact interaction in momentum space is

$$\langle k', 0|V^{\rm IR}_{\rm DVR}|k, 0\rangle = C_{\rm LO} v^{\rm IR}_{\rm DVR}(k') v^{\rm IR}_{\rm DVR}(k). \qquad (26)$$

Figure 3 shows this interaction as a matrix in momentum space. The interaction is very smooth and almost constant, and rapidly approaches zero at the UV cutoff of the finite harmonic oscillator basis with $N = 8$, $\hbar\omega = 22$ MeV. Thus, IR improvement allows us to generate interactions with an accurate IR behavior even for momenta that are much smaller than the IR cutoff of the finite harmonic oscillator basis.

We now turn to the IR improvement of the NLO interaction,

$$V(k', l' = 0; k, l = 0) = C_{\rm NLO}[w(k) + w(k')], \qquad (27)$$

with

$$w(k) \equiv k^2. \qquad (28)$$

Here, $C_{\rm NLO}$ is the coupling strength. The interaction is no longer separable, and the DVR interaction has momentum-space matrix elements

$$\langle k', 0|\hat V_{\rm DVR}|k, 0\rangle = C_{\rm NLO}[w_{\rm DVR}(k) + w_{\rm DVR}(k')] \qquad (29)$$

with

$$w_{\rm DVR}(k) = \sum_{\mu=0}^{N_0} c_{\mu,0} k^2_{\mu,0} \tilde\phi_{\mu,0}(k). \qquad (30)$$

Figure 4 shows the functions $w(k)$ and $w_{\rm DVR}(k)$ as the dash-dotted black and dashed red line, respectively. They coincide at the DVR points (shown as dots).

It is clear that $w_{\rm DVR}$ has the wrong value and the wrong curvature at $k = 0$. This can be corrected by effectively changing the values of the coefficients $c_{N_0-1,0}$ and $c_{N_0,0}$, i.e., the DVR-improved function becomes

$$w^{\rm IR}_{\rm DVR}(k) = \sum_{\mu=0}^{N_0} \bar c_{\mu,0} k^2_{\mu,0} \tilde\phi_{\mu,l}(k) \qquad (31)$$

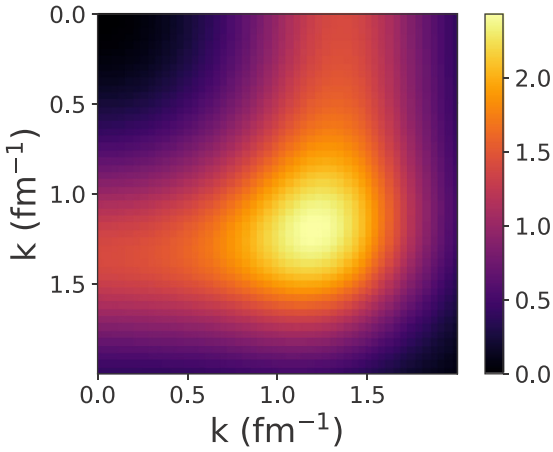

FIG. 5. Momentum space matrix elements $V(k,k') = (k^2 + k'^2)$ for S waves in the model space $N = 8$ and $\hbar\omega = 22$ MeV as a function of the momenta k and k' after IR improvement.

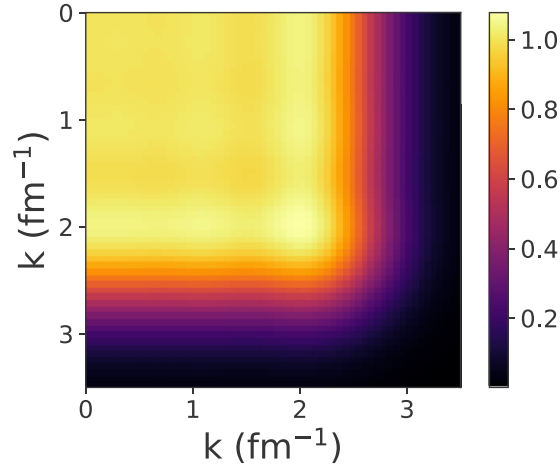

FIG. 6. Momentum space matrix elements $v^{\rm IR}_{\rm DVR}(k)v^{\rm IR}_{\rm DVR}(p)$ in harmonic oscillator model space with $N = 8$ and $\hbar\omega = 22$ MeV as a function of the two incoming Jacobi momenta k and p.

with

$$\begin{aligned}
\bar{c}_{\mu,0} &= c_{\mu,0}, \quad \text{for } \mu = 0,\ldots,N_0-2,\\
\bar{c}_{N_0-1,0} &= \frac{\sum_{\nu=0}^{N_0-2}\tilde{\phi}_{\nu,0}(0)c_{\nu,0}\big(k^2_{N_0,0}-k^2_{\nu,0}\big)-k^2_{N_0,0}}{\tilde{\phi}_{N_0-1,0}(0)\big(k^2_{N_0-1,0}-k^2_{N_0,0}\big)},\\
\bar{c}_{N_0,0} &= \frac{\sum_{\nu=0}^{N_0-2}\tilde{\phi}_{\nu,0}(0)c_{\nu,0}\big(k^2_{N_0-1,0}-k^2_{\nu,0}\big)-k^2_{N_0-1,0}}{\tilde{\phi}_{N_0,0}(0)\big(k^2_{N_0,0}-k^2_{N_0-1,0}\big)}.
\end{aligned} \tag{32}$$

The function $w^{\rm IR}_{\rm DVR}$ from Eq. (31) is shown as a solid blue line in Fig. 4. It agrees at $N-2$ DVR points with $w(k)$ and has the correct IR behavior. The IR improved interaction has matrix elements

$$\langle\phi_{\mu,0}|V^{\rm IR}_{\rm DVR}|\phi_{\nu,0}\rangle = C_{\rm NLO}\bar{c}_{\mu,0}\bar{c}_{\nu,0}\big(k^2_{\mu,0}+k^2_{\nu,0}\big),$$

and these are shown in Fig. 5. It is clear that the IR improvement can be extended to more general interactions.

D. IR improvement of the *NNN* contact

We consider the three-body contact

$$V(k',p';k,p) = C_{NNN} \tag{33}$$

with its LEC C_{NNN}. The momenta k, k' denote the incoming and outgoing relative momentum between particles 1 and 2, respectively, while p, p' are the incoming and outgoing momentum of particle 3 relative to the center of mass of particles 1 and 2, respectively. We note that for a contact interaction the corresponding orbital angular momenta are zero; thus we ignore the orbital angular momentum label in what follows. We also note that the matrix element (33) is not fully antisymmetrized, but this is not relevant here. In what follows, we discuss two different nonlocal regulators in oscillator basis.

1. Cutoff in Jacobi momenta

One possibility is to regulate the incoming Jacobi momenta k and p individually (and similar for the outgoing Jacobi momenta). This approach is somewhat unusual as it corresponds to regulator functions $f(p)f(k)$ that are multiplied with the interaction. In this case, the DVR interaction becomes

$$\begin{aligned}
&\langle k',p'|\hat{V}^{\rm sq}_{\rm DVR}|k,p\rangle\\
&\quad = C^{\rm sq}_{NNN}v_{\rm DVR}(k')v_{\rm DVR}(p')v_{\rm DVR}(k)v_{\rm DVR}(p),
\end{aligned} \tag{34}$$

and $v_{\rm DVR}$ is as in Eq. (23). Thus, the IR improvement of the *NNN* contact is identical to the *NN* contact discussed above, and we have to replace $v_{\rm DVR}(k)$ in Eq. (34) by Eq. (25). Figure 6 plots the function $v^{\rm IR}_{\rm DVR}(k)v^{\rm IR}_{\rm DVR}(p)$ for S waves in both Jacobi momenta in harmonic oscillator model space with $N = 8$ and $\hbar\omega = 22$ MeV. Note that we have renamed the LEC as $C^{\rm sq}_{NNN}$ in Eq. (34) because of the square shape of the interaction in the Jacobi basis.

2. Hyperspherical cutoff

Usually, the cutoff of the *NNN* force is in the hypermomentum; see Refs. [67,85] for examples. We introduce the hyper-radial momentum ρ and the hyperangle α as

$$k = \rho\cos\alpha, \quad p = \rho\sin\alpha. \tag{35}$$

The *NNN* contact is isotropic in hyperspherical coordinates and only depends on the hypermomentum ρ. We recall that the orbital angular momenta corresponding to the Jacobi momenta vanish for the *NNN* contact, and so does the hyperspherical angular momentum. In this special case, the hyperradial wave function of interest is the eigenstate of a six-dimensional harmonic oscillator with vanishing hyperangular momentum, i.e.,

$$\tilde{\Psi}_n(\rho) = \bar{b}^3\sqrt{\frac{2n!}{\Gamma(n+3)}}e^{-\rho^2\bar{b}^2/2}L^2_n(\rho^2\bar{b}^2), \tag{36}$$

and corresponds to the energy $(2n+3)\hbar\omega$. Here, $\bar{b} = \sqrt{\hbar/m\omega}$ is the oscillator length in terms of the nucleon mass m and differs from Eq. (5).

It is straightforward to derive the DVR for the hypermomentum. It is based on the discrete momenta ρ_μ (with $\mu = 0,\ldots,N$), which are the zeros of the Laguerre polynomial

$L^2_{N+1}(\rho^2\bar{b}^2)$. The momentum eigenfunction corresponding to eigenvalue ρ_μ is

$$\Phi_\mu(\rho) = C_\mu \sum_{n=0}^{N} \tilde{\Psi}_n(\rho_\mu)\tilde{\Psi}_n(\rho). \tag{37}$$

Here, C_μ is a normalization constant. Analogous to Eq. (14), we find

$$C_\mu = \frac{\rho_\mu \bar{b}}{\sqrt{(N+3)(N+1)}\tilde{\Psi}_N(\rho_\mu \bar{b})}. \tag{38}$$

The *NNN* contact thus becomes

$$\langle \rho' | U_{\rm DVR} | \rho \rangle = u_{\rm DVR}(\rho') u_{\rm DVR}(\rho) \tag{39}$$

with

$$u_{\rm DVR}(\rho) = \sum_{\mu=0}^{N} C_\mu \tilde{\Phi}_\mu(\rho). \tag{40}$$

As before, this DVR interaction needs IR improvement. We generalize the solution (24) to improve the low-momentum behavior of the DVR interaction at hyperspherical radial momentum $\rho = 0$,

$$\begin{aligned} \bar{C}_\mu &\equiv C_\mu, \quad \text{for } \mu = 0, \ldots, N-1, \\ \bar{C}_N &\equiv \left(1 - \sum_{\nu=0}^{N-1} \tilde{\Phi}_\nu(0) C_\nu\right) \Big/ \tilde{\Phi}_N(0), \end{aligned} \tag{41}$$

and arrive at the IR improved function

$$u^{\rm IR}_{\rm DVR}(\rho) = \sum_{\mu=0}^{N} \bar{C}_\mu \tilde{\Phi}_\mu(\rho). \tag{42}$$

Thus, the IR improved potential is

$$\langle \rho' | U^{\rm IR}_{\rm DVR} | \rho \rangle = C^{\rm tr}_{NNN} u^{\rm IR}_{\rm DVR}(\rho') u^{\rm IR}_{\rm DVR}(\rho). \tag{43}$$

Here $C^{\rm tr}_{NNN}$ is the corresponding coupling strength.

Figure 7 compares Eq. (42) of the IR improved contact (the solid blue line) with the contact in Eq. (40) lacking IR improvement (the dashed red line). Note that the latter exhibits particularly large deviations from a constant value typical for a contact at small momenta below the IR cutoff. This is because the integration measure $d\rho\rho^5$ suppresses low-momentum deficiencies in the usual scalar product.

Our computer codes use the *NNN* potential in Jacobi coordinates as input. For this reason, we need to transform the matrix elements in Eq. (43) to the Jacobi basis. The DVR provides us with a very simple and elegant solution to this problem. Recall that the DVR in the Jacobi momenta provides us with a Gauss-Laguerre integration that becomes exact for polynomials of degree N in k and in p. Thus, the basis functions in Eq. (36) can be exactly integrated, and

$$\langle \phi_{\nu',0}\phi_{\mu',0} | \hat{U}^{\rm IR}_{\rm DVR} | \phi_{\mu,0}\phi_{\nu,0} \rangle = C^{\rm tr}_{NNN} \bar{u}_{\mu'\nu'} \bar{u}_{\mu\nu} \tag{44}$$

with $\bar{u}_{\mu\nu} = c_{\mu,0}c_{\nu,0}u^{\rm IR}_{\rm DVR}(\sqrt{k^2_{\mu,0} + p^2_{\nu,0}})$. We note that the reduced mass is set to m in calculating $c_{\mu,0}$ and $k_{\mu,0}$ here. Figure 8 plots matrix elements of the DVR interaction, given in Eq. (44), in Jacobi momentum space.

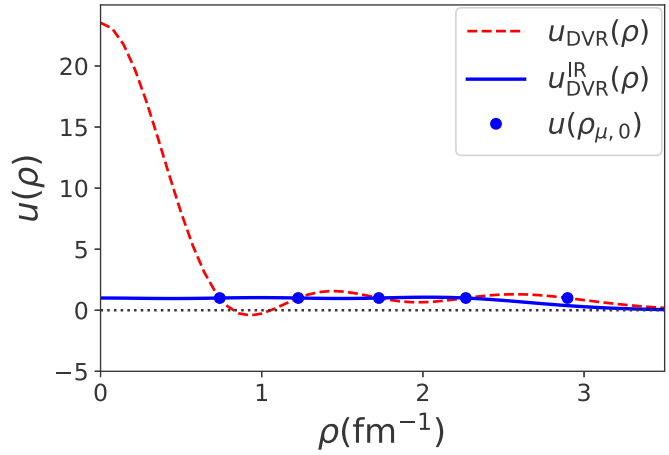

FIG. 7. The solid blue and dashed red curves show the three-nucleon contact in the DVR basis in hyperspherical coordinates with and without IR improvement. The former is close to $u(\rho) = 1$ at low momentum. The solid blue dots represent the DVR momenta ρ_μ for $\mu = 0, \ldots, N$ when $N = 8$ and $\hbar\omega = 22$ MeV.

Closer inspection reveals that the overlap between the hyper-radial wave function $\Psi_N(\rho)$ and the radial wave functions $\tilde{\psi}_{i,0}(k)\tilde{\psi}_{j,0}(p)$ vanishes for $i + j > N$. Thus, the hyperspherical cutoff corresponds to a "triangular" cutoff in the oscillator basis of the Jacobi coordinates. For this reason, the LEC of the *NNN* contact in Eq. (43) carries the subscript "tr". In what follows we will employ the hyperspherical formulation of *NNN* potential unless specified otherwise.

E. Discussion

Let us briefly summarize and discuss the main results of this section. We introduced a momentum-space DVR in the harmonic oscillator basis as an efficient tool to implement an EFT. The DVR potential agrees with the momentum-space potential only at a set of discrete momenta. The

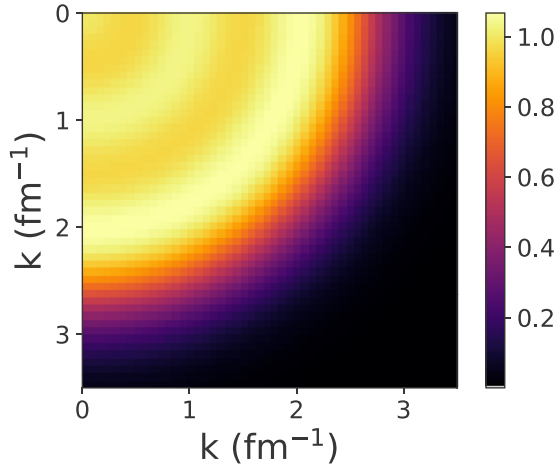

FIG. 8. Size of momentum space matrix elements $\bar{u}(k, p) = c_{\mu,0}c_{\nu,0}u^{\rm IR}_{\rm DVR}(\sqrt{k^2 + p^2})$ in harmonic oscillator model space $N = 8$, $\hbar\omega = 22$ MeV, $l_1, l_2 = 0$. x and y axes represent Jacobi momenta in $\rm fm^{-1}$.

low-momentum behavior of the DVR potential can be corrected such that it agrees with the momentum-space potential at zero momentum. We have shown how to implement these IR improvements for *NN* and *NNN* potentials.

One may wonder whether the IR improvement is really necessary. Clearly, if one aims at an EFT that is valid at lowest momenta, the IR improvement cannot be avoided. As we will see below, this is particularly so when LECs of the EFT potential are adjusted to the effective range expansion. The works [43,44] showed that a lack of IR improvement leads to oscillations in phase shifts, which made it difficult to adjust the interaction to data. However, it is not clear how much structure calculations of nuclei [24,26] have been impacted by the use of a finite harmonic oscillator basis without IR improvements. It could be that observables such as ground-state energies and radii of well-bound nuclei are not sensitive to the details of the underlying interaction at lowest momenta. The argument is that the relevant momentum scale, i.e., the momentum corresponding to the smallest separation energy, often exceeds the IR cutoff of the oscillator basis; see Refs. [86,87] and Appendix H.

Many details regarding the implementation of an EFT as a DVR in the oscillator basis are presented in the appendixes of this work. There we show that a DVR can be implemented in many ways (see Appendix B), that the IR improvement is a systematic and controlled approximation (see Appendix C), that there are simple scaling laws for the resulting DVR interactions (see Appendix D), that the Wigner bound is obeyed (see Appendix E), and that regulator differences, i.e., different combinations of $\hbar\omega$ and N with the same UV cutoff Λ, are higher-order effects (see Appendix F). We also explore the effects of truncations of *NNN* forces in Appendix G, and finally show in Appendix H that IR extrapolations work well in the DVR approach.

III. CALIBRATION AND RESULTS FOR ^{3}H AND ^{3,4}He

A. Atomic nuclei

In this section, we adjust the LECs in pion-less EFT to data. For atomic nuclei, we will use the deuteron binding energy, the effective-range expansion of the S-wave phase shifts, and the phase shifts of the charge-dependent (CD)–Bonn potential [88] to constrain the LECs of the *NN* interaction. We note that the CD-Bonn potential reproduces phase shifts in the singlet and triplet S channels that are of similar quality as the Nijmegen multi-energy phase shift analysis; see, e.g., Figs. 6 and 7 in Ref. [88]. The *NNN* contact will be adjusted to reproduce the triton binding energy. For the fits to phase shifts the χ^2 objective function contains NLO uncertainty estimates as reciprocal weights such that low-energy "data" are weighted highest.

To compute phase shifts in the harmonic oscillator basis, we follow Ref. [46], which is based on the J-matrix approach [45]. For the computation of binding energies we proceed as follows. For the interaction we will employ a model space with $N = 8$. The Hamiltonian, i.e., the sum of kinetic energy and the interaction, will be evaluated in model spaces of size $N = 8, 10, 12, \ldots$. For the interaction, the matrix elements between states with $N > 8$ are zero. Thus, UV convergence is achieved by construction. The increase of the model space for the kinetic energy yields IR convergence; see Ref. [43] for details. In what follows, we report virtually converged results for nuclei with mass numbers $A = 2, 3, 4$. We vary the oscillator spacing to probe the cutoff dependence of our results.

TABLE I. The leading order LECs $\tilde{C}_{^3s_1}$ and $\tilde{C}_{^1s_0}$ (both in 10^{-5} MeV^{-2}), and c_E (dimensionless) for atomic nuclei (with nucleon mass $m = 939$ MeV) for different momentum cutoffs Λ (in MeV) obtained from varying the oscillator frequency $\hbar\omega$ (in MeV), for interactions in a model space with $N = 8$.

$\hbar\omega$	Λ	$\tilde{C}_{^3s_1}$	$\tilde{C}_{^1s_0}$	c_E
5	232.35	−1.006 988	−0.597 220	−0.163 306
10	328.59	−0.624 098	−0.431 559	−0.671 882
22	487.38	−0.379 465	−0.296 100	−0.238 514
40	657.19	−0.266 381	−0.221 703	−0.091 625

At LO we have two LECs associated with *NN* contact interactions and one for the *NNN* contact. In the $^3S_1$ partial wave, the LEC is adjusted to reproduce the deuteron binding energy. We would like to remind the readers that bound-state properties such as the deuteron binding energy or its radius are governed by low energy and long wavelength physics. Therefore, from an EFT point of view, they are as suited as more conventional observables like scattering length and effective range to obtain LECs. For example, an interaction in the model space with $N = 8$ and $\hbar\omega = 22$ MeV, when fit to deuteron binding energy, yields the scattering length $a = 4.71$ fm, which is within LO uncertainties, i.e., about 30% of the actual value of about 5.4 fm. The coupling strength in the singlet S channel for the *NN* contact is adjusted to the neutron-proton (np) phase shifts of the CD-Bonn potential for energies $E_{\rm rel} \in [0.01, 0.1]$ MeV. The predicted value for the triplet S scattering length agrees with data within 30%, which is what we expect from simple error estimates discussed below. Table I shows the values of the LECs at LO for potentials defined in model spaces with $N = 8$ for different cutoffs.

We note that the LECs $\tilde{C}_{^3s_1}$ and $\tilde{C}_{^1s_0}$ approximately obey the relation $C_{\rm LO} \propto (\hbar\omega)^{-1/2}$. This is a consequence of the deuteron's weak binding; see Appendix D for details. We also note that the LECs of the *NN* interaction are consistent with analytical results. To see this, we consider the LO potential

$$V(k', k) = C_0 v(k', \Lambda) v(k, \Lambda). \tag{45}$$

Here, $v(k', \Lambda)$ is the regulator function and Λ is the cutoff. For the step-function regulator $v(k, \Lambda) = \Theta(\Lambda - k)$ we have

$$C_0 \approx -\frac{2\pi^2}{m\Lambda}\frac{4\pi}{(2\pi)^3}, \tag{46}$$

valid for $\Lambda \gg \kappa, a^{-1}$ where κ is the binding momentum and a the scattering length. Similarly, for a Gaussian regulator $v(k, \Lambda) = e^{-(1/2)(k^2/\Lambda^2)}$ one has

$$C_0 \approx -\frac{4\pi\sqrt{\pi}}{m\Lambda}\frac{4\pi}{(2\pi)^3}, \tag{47}$$

TABLE II. The next-to-leading order LECs $\tilde{C}_{^3s_1}$ and $\tilde{C}_{^1s_0}$ (both in 10^{-5} MeV^{-2}), and $C_{^3s_1}$ and $C_{^1s_0}$ (both in 10^{-10} MeV^{-4}), and c_E (dimensionless) for atomic nuclei (with nucleon mass $m = 939$ MeV) for different momentum cutoffs Λ (in MeV) obtained from varying the oscillator frequency $\hbar\omega$ (in MeV), for interactions in a model space with $N = 8$.

$\hbar\omega$	Λ	$\tilde{C}_{^3s_1}$	$C_{^3s_1}$	$\tilde{C}_{^1s_0}$	$C_{^1s_0}$	c_E
5	232.35	−1.001 248	−0.039 732	−0.718 772	1.124 941	0.533 367
10	328.59	−0.919 696	1.078 144	−0.588 224	0.725 705	−0.274 206
22	487.38	−0.809 378	0.772 254	−0.612 966	0.727 724	−0.008 170
40	657.19	−0.866 529	0.689 544	−0.605 710	0.590 509	−0.061 330

under the same conditions.[1] For $\Lambda = 487$ MeV and $m = 939$ MeV we find $C_0 \approx -0.22 \times 10^{-5}$ MeV^{-2} for the sharp cutoff, and $C_0 \approx -0.25 \times 10^{-5}$ MeV^{-2} for the Gaussian regulator. These results are similar in size to what is reported in Table I for the same cutoff. Thus, the results from our EFT constructed in the harmonic oscillator basis are fully compatible with expectations from a momentum-space EFT.

We now turn to the NLO potential. Here, we employ three LECs from the LO contacts, and two additional LECs from the NLO *NN* contact interaction in *S* waves. We determine the LECs using nonperturbative solvers for the *J* matrix and the Hamiltonian eigenvalues. In the triplet *S* channel the LECs are inferred from the deuteron binding energy and its radius (1.976 fm). Also, the reproduction of the scattering length and effective range from such a potential can clearly be inferred from the lower panel in Fig. 9. The results are similar in quality to those by Chen *et al.* [89]. In the singlet *S* channel, the LECs are adjusted to *np* phase shifts of the CD-Bonn potential for energies $E_{\rm rel} \in [0.01, 0.1]$ MeV. The *NN* interaction at NLO determines the scattering lengths and the effective range r_0. Once the *NN* potential is fixed at NLO, the LEC for the *NNN* contact is adjusted to reproduce the triton binding energy. The results for the LECs are presented in Table II.

Figure 9 shows the phase shifts from pion-less EFT at LO (blue dot-dashed line) and NLO (red dashed line), and compares them to those of the CD-Bonn potential (black line). The LO potentials reproduce phase shifts for momenta $p_{\rm rel} \lesssim {a_{s,t}}^{-1}$, while the NLO interactions extends the range to $p_{\rm rel} \lesssim {r_{s,t}}^{-1}$. Results are consistent with our expectation from EFT as confirmed by blue and red shaded areas which correspond to EFT uncertainty in phase shift at LO $[\mathcal{O}(\frac{p_{\rm rel}}{\Lambda})]$ and NLO $[\mathcal{O}(\frac{p_{\rm rel}^2}{\Lambda^2})]$, respectively. In addition, the LO and NLO phase shifts at different cutoffs lie within the estimated error bands. We note that the estimate of uncertainty in Fig. 9 at each order is scaled by a constant factor of natural size such that the uncertainty in phase shifts at LO spans the actual data and NLO uncertainty (as done in Ref. [90]). This constant factor is observable dependent and can be understood as the largest $|c_k|$ in Eq. (48). The phase shift plots illustrate the quality of the IR improved potentials. The oscillations that were observed in Refs. [43,44] are much reduced.

Our LO results (binding energies and point-proton radii) for the light nuclei ^{3}H and ^{3,4}He, computed with a translationally invariant no-core-shell model [91], are collected in Table III. The results for *NN* interaction alone exhibit a strong cutoff dependence. This dependence becomes much weaker once the *NNN* contact is included. At LO with *NNN* forces included, the nucleus ^{4}He is underbound. This result is consistent with the results reported by Kirscher *et al.* [15], also obtained at lower cutoffs (though the authors expressed some doubts regarding the convergence of their calculation).

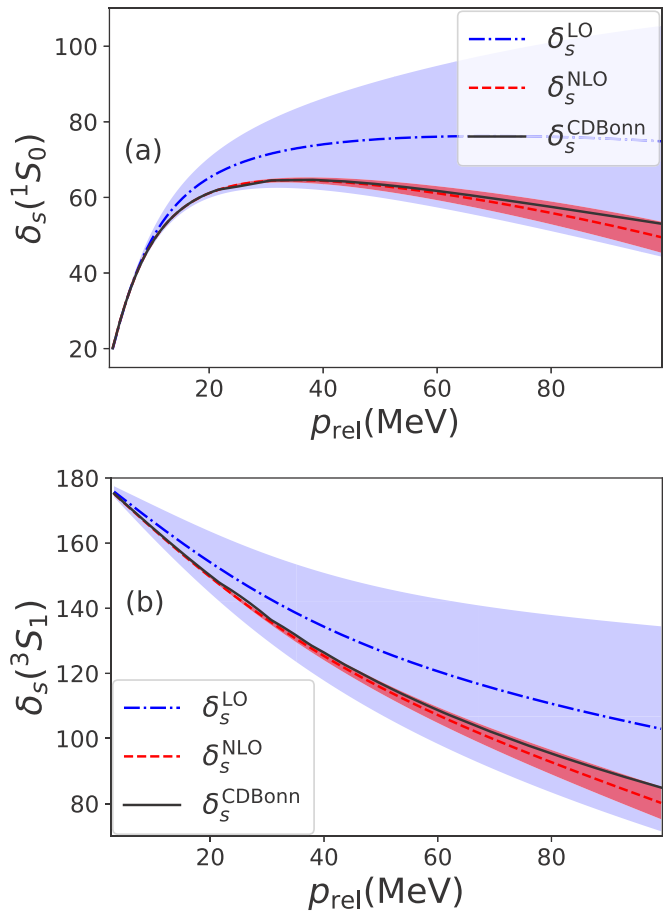

FIG. 9. Phase shifts in the partial waves $^1S_0$ (a) and $^3S_1$ (b) from IR improved potentials at NLO (red dashed) and LO (blue dot-dashed), respectively, in a model space $N = 8$, $\hbar\omega = 22$ MeV, $l = 0$. The black curves shows the neutron-proton phase shifts of the CD-Bonn potential. The blue (biggest) and red (smallest) shaded area correspond to EFT uncertainty at LO and NLO, respectively.

[1]These results are obtained in momentum space with the momentum integration $\int_0^\infty dk k^2$ as used in the harmonic oscillator EFT. They differ by a factor $4\pi/(2\pi)^3$ from results obtained with the usual integration measure $\int d^3k/(2\pi)^3$.

TABLE III. Binding energies and point-proton radii of $A \leqslant 4$ nuclei using *NN* and *NN* + *NNN* pion-less EFT interactions at LO and defined in model space $N = 8$.

LO *NN*							
$\hbar\omega$	Λ	$E(^3\mathrm{H})$	$r(^3\mathrm{H})$	$E(^3\mathrm{He})$	$r(^3\mathrm{He})$	$E(^4\mathrm{He})$	$r(^4\mathrm{He})$
5	232.35	8.65	1.78	8.04	1.89	26.81	1.79
10	328.59	13.34	1.31	12.49	1.37	45.45	1.28
22	487.38	23.69	0.91	22.46	0.95	88.06	0.87
40	657.19	38.31	0.69	36.65	0.71	149.88	0.65
LO *NN* + *NNN*							
$\hbar\omega$	Λ	$E(^3\mathrm{H})$	$r(^3\mathrm{H})$	$E(^3\mathrm{He})$	$r(^3\mathrm{He})$	$E(^4\mathrm{He})$	$r(^4\mathrm{He})$
5	232.35	8.482	1.79	7.87	1.90	26.05	1.79
10	328.59	8.482	1.46	7.71	1.60	22.40	1.44
22	487.38	8.482	1.29	7.54	1.46	17.66	1.46
40	657.19	8.482	1.23	7.41	1.42	17.55	1.42

Table IV shows our results for light nuclei at NLO. We note that the NLO results for *NN* interactions alone are close to the data, i.e., $E(^3\mathrm{H}) = 8.48$ MeV, $E(^3\mathrm{He}) = 7.5$ MeV, and $E(^4\mathrm{He}) = 28.5$ MeV, and depend very weakly on the cutoff over the considered range of cutoffs. Similar comments apply to the radii. Including the *NNN* contact further reduces the cutoff dependence, and the ^{4}He nucleus is close to its physical point. Our finite oscillator regulated *NN* interaction breaks down at a UV cutoff of about 650 MeV (see Appendix E). Therefore we limit our calculations to moderate cutoffs.

Let us discuss theoretical uncertainties. The three contributions to the error budget are (i) neglected higher-order terms of the interaction, (ii) uncertainties in the LECs due to uncertainties of the input, and (iii) the convergence of the calculations with respect to the model space. For the nuclei discussed here, only the first contribution is relevant. The third contribution to the uncertainties yields very small corrections as shown in Appendix H.

Based on the power counting in pion-less EFT, the uncertainty for observable X is expected to be of the form [92]

$$\Delta X = X_0(c_1 Q + c_2 Q^2 + \cdots), \tag{48}$$

TABLE IV. Binding energies and point-proton radii of $A \leqslant 4$ nuclei using *NN* and *NN* + *NNN* pion-less EFT interactions at NLO and defined in model space $N = 8$.

NLO *NN*							
$\hbar\omega$	Λ	$E(^3\mathrm{H})$	$r(^3\mathrm{H})$	$E(^3\mathrm{He})$	$r(^3\mathrm{He})$	$E(^4\mathrm{He})$	$r(^4\mathrm{He})$
5	232.35	7.94	1.82	7.35	1.97	25.03	1.80
10	328.59	10.11	1.49	9.34	1.61	36.24	1.34
22	487.38	8.62	1.62	7.90	1.82	30.39	1.41
40	657.19	8.97	1.62	8.30	1.77	29.95	1.53
NLO *NN* + *NNN*							
$\hbar\omega$	Λ	$E(^3\mathrm{H})$	$r(^3\mathrm{H})$	$E(^3\mathrm{He})$	$r(^3\mathrm{He})$	$E(^4\mathrm{He})$	$r(^4\mathrm{He})$
5	232.35	8.482	1.80	7.88	1.93	27.52	1.79
10	328.59	8.482	1.59	7.75	1.75	27.30	1.43
22	487.38	8.482	1.63	7.77	1.83	29.30	1.44
40	657.19	8.482	1.65	7.82	1.82	27.35	1.58

TABLE V. Relevant values of physical and lattice QCD data (all in MeV), namely the pion mass m_π, the nucleon mass m, the dineutron binding energy B_{nn}, the deuteron binding energy B_d, the triton binding energy B_t, the singlet and triplet scattering lengths ${}^{np}a_s$ and a_t, respectively, the singlet and triplet effective ranges ${}^{np}r_s$ and r_t, respectively.

	Nature	Lattice
m_π	139.5 ± 0.1 [95]	806. ± 1 [10]
m	939. ± 1 [96]	1634. ± 18 [10]
B_{nn}		15.9 ± 4 [10]
B_d	2.2245	19.5 ± 5 [10]
B_t	8.482 [97]	53.9 ± 10.7 [10]
${}^{np}a_s{}^{-1}$	−8.31 [98]	84.7 ± 18 [94]
${}^{np}r_s{}^{-1}$	71.75 [98]	174.6 ± 25 [94]
$a_t{}^{-1}$	36.4 [98]	108. ± 13 [94]
$r_t{}^{-1}$	112.18 [98]	217.8 ± 46 [94]

where $Q = p_F/\Lambda_b$ is the typical momentum ratio, expressed in terms of the Fermi momentum p_F and the breakdown scale Λ_b. The coefficients c_k are parameters, expected to be of natural size. The free Fermi gas estimate

$$\frac{E}{A} = \frac{3}{10}\frac{p_F^2}{m} \tag{49}$$

relates the average binding energy to the Fermi momentum, yielding $p_F \approx 150$ MeV for ^{4}He. Around the UV cutoff $\Lambda \approx 650$ MeV, we are unable to reproduce the effective range of the *NN* interaction and therefore we consider it to be the breakdown scale (see Appendix E for details) giving a very conservative $Q \approx 1/3$. Consequently, the uncertainty in the binding energy of ^{4}He at LO is estimated to be about 30% i.e., $\Delta E_{\mathrm{LO}}(^4\mathrm{He}) \approx 8$ MeV. Similarly, at NLO it is estimated to be around 10% or $\Delta E_{\mathrm{NLO}}(^4\mathrm{He}) \approx 3$ MeV. These simple estimates are also consistent with the change of the α-particle binding energy resulting from the variation of the UV cutoff Λ at each order. Moreover, the LO and NLO binding energies overlap after including the discussed uncertainties. The ^{4}He binding exhibits a nonmonotonic variation as the cutoff is increased. A similar behavior was shown in Fig. 14 of Ref. [93], and this can probably be attributed to the small cutoff range. We note that the Wigner bound prevents us from fitting the effective range expansion for cutoffs exceeding 650 MeV; see Appendix E for details. We also note that the experimental binding energy of ^{4}He (28.3 MeV) falls within the uncertainties of our NLO result.

B. Lattice nuclei

For lattice nuclei we optimize the LECs using the binding energies of the deuteron and the dineutron, the effective range expansion, and the triton binding energy from lattice QCD data in Refs. [10,94]. The relevant lattice data are compiled in Table V and compared to the physical point.

At LO, the LECs for the *NN* contacts are adjusted to the central values of the binding energies of the deuteron and the dineutron. The *NNN* contact is adjusted to the central value of the triton binding energy. The results are shown in Table VI.

TABLE VI. The leading order LECs $\tilde{C}_{^3s_1}$ and $\tilde{C}_{^1s_0}$ (both in 10^{-5} MeV^{-2}), and c_E (dimensionless) for lattice nuclei (with nucleon mass $m = 1634$ MeV) for different momentum cutoffs Λ (in MeV) obtained from varying the oscillator frequency $\hbar\omega$ (in MeV), for interactions in a model space with $N = 8$.

$\hbar\omega$	Λ	$\tilde{C}_{^3s_1}$	$\tilde{C}_{^1s_0}$	c_E
5	306.52	−1.013 613	−0.904 019	−1.731 712
10	433.48	−0.502 300	−0.460 312	−0.433 930
22	642.96	−0.251 429	−0.236 527	−0.086 293
40	866.97	−0.158 373	−0.151 299	−0.025 688

For the NLO potential, we use the data on the effective range expansion parameters calculated by Beane *et al.* [94]. In that work, the location of the bound state was used to constrain the effective range expansion $k \cot \delta$, followed by a two-parameter fit to determine the scattering length and the effective range. We optimize the NLO interaction by performing a simultaneous fit to the binding energy and the effective range expansion in the singlet and triplet S channels. We determine the *NNN* contact interaction strength by fitting it to the triton binding energy. Table VII contains the LECs at NLO for different cutoffs.

Figure 10 shows the phase shifts for lattice nuclei obtained at LO (dashed-dotted line) and at NLO (dashed lines). The input from the effective range expansion (3) is shown as a solid line with grey uncertainty estimates from lattice QCD. The blue (biggest) and red (smallest) shaded area correspond to the EFT uncertainties at LO and NLO, respectively, once the interaction is optimized to reproduce the central values of binding energy and effective range expansion parameters in each channel. We see that the EFT agrees with the input data at NLO over a considerable range of momenta.

We turn to the calculations of light lattice nuclei. Table VIII shows the LO results for the binding energies and point-proton radii of lattice nuclei. At LO, the *NN* interaction yields binding energies for ^{4}He that vary by a factor of 2 over the cutoff range. This dependence is reduced once the *NNN* contact is added.

We turn to NLO calculations of light lattice nuclei. The upper and lower parts of Table IX show the NLO results for binding energies and point-proton radii with *NN* potentials only and with the *NNN* contact included, respectively. The cutoff dependence is strong for *NN* forces alone and much reduced for the complete calculation including *NNN* forces. We note that with the full LO and NLO interaction, our

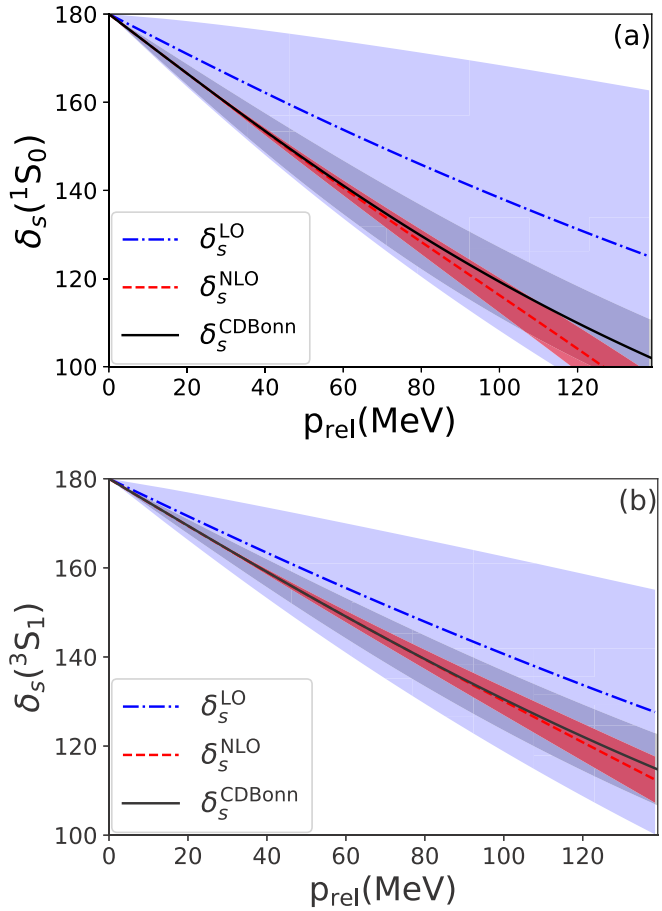

FIG. 10. Phase shifts for lattice nucleons at $m_\pi = 806$ MeV in the partial waves $^1S_0$ (a) and $^3S_1$ (b) from IR improved potentials at NLO (red dashed) and LO (blue dot-dashed), respectively, in a model space $N = 8$, $\hbar\omega = 22$ MeV. The black curves shows the effective range expansion from lattice QCD [94] with corresponding systematic plus statistical uncertainties shown as a grey band. The blue (biggest) and red (smallest) shaded area correspond to EFT uncertainties at LO and NLO, respectively, once the interaction is optimized to the central values of the binding energy and the effective range expansion parameters from lattice QCD results by Beane *et al.* [94].

^{4}He binding energy is consistent with the lattice QCD result (107 ± 34 MeV) by Beane *et al.* [10].

We note that uncertainty in lattice QCD input is much larger than the effects from inclusion of the Coulomb interaction. For instance, the Coulomb interaction changes the

TABLE VII. The next-to-leading order LECs $\tilde{C}_{^3s_1}$ and $\tilde{C}_{^1s_0}$ (both in 10^{-5} MeV^{-2}), and $C_{^3s_1}$ and $C_{^1s_0}$ (both in 10^{-10} MeV^{-4}), and c_E (dimensionless) for lattice nuclei (with nucleon mass $m = 1634$ MeV) for different momentum cutoffs Λ (in MeV) obtained from varying the oscillator frequency $\hbar\omega$ (in MeV), for interactions in a model space with $N = 8$.

$\hbar\omega$	Λ	$\tilde{C}_{^3s_1}$	$C_{^3s_1}$	$\tilde{C}_{^1s_0}$	$C_{^1s_0}$	c_E
5	306.52	−0.736 443	−1.034 289	−1.216 789	1.180 748	−1.719 559
10	433.48	−0.632 458	0.246 988	−0.854 814	0.760 970	−0.430 321
22	642.96	−0.449 998	0.177 545	−0.691 412	0.423 704	−0.076 720
40	866.97	−0.387 445	0.118 521	−0.853 482	0.471 613	−0.106 436

TABLE VIII. Binding energies and point-proton radii of $A = 3, 4$ lattice nuclei at $m_\pi = 806$ MeV using *NN* and *NN* + *NNN* pion-less EFT interactions at LO in model space $N = 8$.

LO *NN*							
$\hbar\omega$	Λ	$E(^3\mathrm{H})$	$r(^3\mathrm{H})$	$E(^3\mathrm{He})$	$r(^3\mathrm{He})$	$E(^4\mathrm{He})$	$r(^4\mathrm{He})$
5	306.52	64.3	1.57	64.5	1.57	142.7	1.62
10	433.48	76.6	1.13	75.6	1.13	177.5	1.17
22	642.96	99.1	0.78	97.6	0.79	249.6	0.80
40	866.97	127.4	0.60	125.5	0.60	344.7	0.60
LO *NN* + *NNN*							
$\hbar\omega$	Λ	$E(^3\mathrm{H})$	$r(^3\mathrm{H})$	$E(^3\mathrm{He})$	$r(^3\mathrm{He})$	$E(^4\mathrm{He})$	$r(^4\mathrm{He})$
5	306.52	53.9	1.55	53.1	1.55	98.9	1.57
10	433.48	53.9	1.13	52.9	1.13	88.5	1.15
22	642.96	53.9	0.84	52.5	0.85	70.8	1.05
40	866.97	53.9	0.72	52.2	0.74	68.3	1.09

binding energy of lattice ^{4}He nucleus from 90.7 to 89.7 MeV at $\hbar\omega = 22$ MeV. Therefore, at the current level of precision we do not worry that the input lattice QCD results from Ref. [10] do not include the Coulomb photon exchange between protons on a lattice.

Let us also discuss uncertainties for lattice nuclei. As we were not able to fit binding energies and the effective range expansions simultaneously at $\hbar\omega = 70$ MeV, we infer a physical breakdown scale $\Lambda_b \approx 1150$ MeV. From the free Fermi gas estimate (49) we find $p_F \approx 370$ MeV based on ^{4}He. We assume a conservative $Q = p_F/\Lambda_b \approx 0.4$, and using Eq. (48) yields the uncertainty $\Delta E_{\mathrm{NLO}}(^4\mathrm{He}) \approx 15$ MeV at NLO for the binding energy of the α particle. Small changes in binding energies with variation in UV cutoff are also consistent with the above estimates. The major uncertainty, however, comes from the large uncertainties in the input lattice QCD data. Using the NLO interaction with *NN* and *NNN* forces at $\hbar\omega = 10$ MeV, for instance, yields $E(^4\mathrm{He}) = 90 \pm 40$ MeV when the LECs are varied within lattice QCD uncertainties. For the heavier lattice nuclei discussed below, we restrict our discussion of uncertainties to the case where LECs are fit to central values of the lattice QCD data in Table V.

TABLE IX. Binding energies and point-proton radii of $A = 3, 4$ lattice nuclei at $m_\pi = 806$ MeV using *NN* and *NN* + *NNN* pion-less EFT interactions at NLO in model space $N = 8$.

NLO *NN*							
$\hbar\omega$	Λ	$E(^3\mathrm{H})$	$r(^3\mathrm{H})$	$E(^3\mathrm{He})$	$r(^3\mathrm{He})$	$E(^4\mathrm{He})$	$r(^4\mathrm{He})$
5	306.52	65.2	1.57	64.4	1.57	142.5	1.61
10	433.48	75.8	1.12	74.8	1.13	176.3	1.16
22	642.96	85.4	0.84	84.0	0.88	217.2	0.82
40	866.97	64.6	1.07	63.7	1.21	139.9	1.23
NLO *NN* + *NNN*							
$\hbar\omega$	Λ	$E(^3\mathrm{H})$	$r(^3\mathrm{H})$	$E(^3\mathrm{He})$	$r(^3\mathrm{He})$	$E(^4\mathrm{He})$	$r(^4\mathrm{He})$
5	306.52	53.9	1.55	53.1	1.55	99.0	1.55
10	433.48	53.9	1.14	52.9	1.16	89.9	1.17
22	642.96	53.9	1.04	52.7	1.13	89.7	1.34
40	866.97	53.9	1.17	53.1	1.29	109.7	1.33

IV. RESULTS FOR ^{16}O AND ^{40}Ca

We compute the nuclei ^{16}O and ^{40}Ca with the coupled-cluster method [24,99,100], performed in the coupled-cluster singles and doubles (CCSD) approximation. The coupled-cluster method creates a similarity-transformed Hamiltonian whose vacuum and ground state is a product state. The pion-less EFT at NLO does not include spin-orbit forces, and the coupled-cluster method produces converged results for nuclei ^{4}He, ^{16}O, and ^{40}Ca because the reference product state for these nuclei exhibit the usual shell closures of the harmonic oscillator. We find that the atomic nuclei ^{16}O and ^{40}Ca are not bound with respect to decay into ^{4}He nuclei using our LO interaction. This is consistent with previous results: Stetcu *et al.* [18] found that ^{6}Li is not bound with respect to ^{4}He at LO, and similar results were also found for lattice nuclei [12]. For these reasons, we report only results at NLO, which do not exhibit this shortcoming. The *NNN* potential is employed in the normal-ordered two-body approximation [101], i.e., it contributes to the vacuum energy of the Hartree-Fock reference, and to the normal-ordered one-body and two-body matrix elements. This approximation is accurate for chiral potentials where *NNN* forces do not enter at LO [102].

The coupled-cluster method employs a translationally invariant intrinsic Hamiltonian

$$H = T - T_{\mathrm{cm}} + V_{NN} + V_{NNN}. \tag{50}$$

Here, T denotes the total kinetic energy and T_{cm} denotes the kinetic energy of the center of mass. We note that the Hamiltonian (50) does not reference the center-of-mass coordinate. This is crucial because the many-body system is solved in the laboratory system using second quantization. While the single-particle states are not eigenstates of the total momentum, the eigenstates of the Hamiltonian (50) factor to a very good approximation into an intrinsic wave function and a Gaussian for the center-of-mass coordinate [103].

We remind the readers that interactions were tailored to the oscillator basis with a maximum energy $N\hbar\omega$ in Jacobi coordinates. The number of matrix elements increases significantly when transforming from the center-of-mass coordinates to the single-particle basis in the laboratory system, and *NNN* forces can become a bottleneck in the computation of heavy nuclei. In practical calculations the number of matrix elements in the laboratory oscillator basis needs to be limited by imposing a truncation on the maximum energies $N_1\hbar\omega$ and $N_3\hbar\omega$ of a single particle and of three particles, respectively. The *NNN* interaction will be cut at N_3, while the relative kinetic energy and the *NN* potentials are limited by N_1 for each of the two nucleons. In what follows, we study how the results stabilize as N_1 and N_3 are increased.

A. Atomic nuclei

As a check on the quality of the CCSD approximation, we also computed the binding energy of ^{4}He and found 27.5, 27.2, 29.0, and 27.5 MeV for the interactions with $N = 8$ and $\hbar\omega = 5$, 10, 22, and 40 MeV, respectively. These results are in good agreement with the virtually exact no-core shell-model (NCSM) results presented in Table IV; they suggest that the

TABLE X. Binding energy of ^{16}O, ^{40}Ca for model space truncations as indicated, as a function of the cutoff Λ (or the oscillator spacing $\hbar\omega$). All quantities in units of MeV. A star (*) indicates that the energy is approximate and did not yet converge after 1000 iterations of the CCSD equations.

$\hbar\omega$	Λ	^{16}O		^{40}Ca	
		$N_1, N_3 = 12$	$N_1, N_3 = 14$	$N_1, N_3 = 12$	$N_1, N_3 = 14$
5	232.35	174.1	174.8	562.5	569.2
10	328.59	136.8	136.2	421.8	415*
22	487.38	143.1	143.1	405.8	405.8
40	657.19	144.7	146.2	372.2	400.0

normal-ordered two-body approximation of the *NNN* force is accurate. The small differences of about 1% between CCSD and NCSM results is most likely due to neglected triples excitations. For a light nucleus such as ^{4}He, the convergence with respect to N_3 is rapid and easily achieved.

The NLO results for ^{16}O and ^{40}Ca are shown in Table X. For the larger cutoff values, the NLO binding energies are within 20% of the experimental values of about 128 and 342 MeV for ^{16}O and ^{40}Ca, respectively. The differences between our NLO results and experimental data seem roughly consistent with EFT expectations. The computation also revealed that only about 10% of the binding energy is correlation energy, i.e., the difference between the coupled cluster and Hartree-Fock results. This small fraction is possibly due to the absence of any mixing between S and D waves. We note that the convergence with respect to the three-body energy N_3 is excellent for $\hbar\omega = 22$ MeV, but slower for the other oscillator spacings. For these latter oscillator spacings we also observe that the N_3 convergence is slower for ^{40}Ca than for ^{16}O. The associated uncertainty is highest at $\hbar\omega = 40$ MeV, being about 10%. We note that ^{4}He is virtually converged at all oscillator spacings. We can only speculate why the N_3 convergence is fastest for $\hbar\omega = 22$ MeV: perhaps this frequency is close to that of the Gaussian center-of-mass wave function, but this warrants more investigation.

Let us also discuss the consistency of our results. At lowest cutoffs, binding energies are largest, and ^{40}Ca has a binding energy per nucleon of about $E/A \approx 14$ MeV at $\hbar\omega = 5$ MeV. In a free Fermi gas this leads to a Fermi momentum of $k_F \approx 210$ MeV. This is marginally below the cutoff of $\Lambda \approx 232$ MeV at $\hbar\omega = 5$ MeV. Thus, it is probably safest to limit our discussion of results to the calculations involving oscillator spacings $\hbar\omega \geqslant 10$ MeV. We note that these results also exhibit a smaller cutoff dependence. Our results show that pion-less EFT binds ^{16}O and ^{40}Ca at about 9 and 10 MeV per nucleon, respectively. Interestingly, these binding energies are close to results from a chiral EFT at NLO [43]. Figure 11 shows binding energies as a function of the UV cutoff, and the results at the smallest cutoff are probably inconsistent because of the proximity of the Fermi momentum.

We use the results of ^{16}O and ^{40}Ca at $\hbar\omega = 22$ MeV to compute the volume, surface, and Coulomb parameters a_V, a_S, a_C, respectively, of the Bethe-Weizsäcker formula

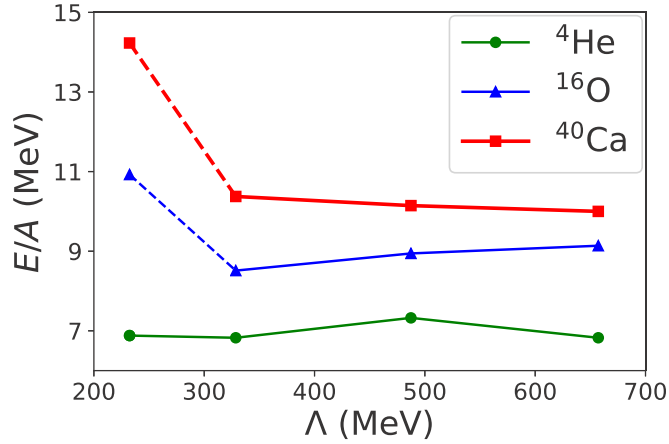

FIG. 11. Binding energy per nucleon for atomic ^{16}O (blue triangles), ^{40}Ca (red squares) nuclei against UV cutoff of the NLO interaction in the model space $N = 8$, $l = 0$ from coupled cluster calculations.

$$E(A) = a_V A - a_S A^{2/3} - a_C \frac{Z^2}{A^{1/3}}, \tag{51}$$

which models the energy of a liquid drop. The liquid drop model addresses bulk properties of nuclear binding. This classical model does not include effects of nuclear shell structure, and is not really applicable to light nuclei such as ^{4}He. Thus, solving Eq. (51) using only doubly magic nuclei might not reproduce the known values obtained from a global fit ($a_V = 15.49$ MeV, $a_S = 17.23$ MeV, $a_C = 0.693$ MeV). Indeed, the fit to the experimental data for ^{4}He, ^{16}O, and ^{40}Ca yields $a_V = 9.2$ MeV, $a_S = 3.4$ MeV, and an unphysical negative value for the Coulomb parameter. As ^{4}He is probably too light to perform a three parameter fit of a bulk formula, and we are limited to doubly magic nuclei, we only use our results for ^{16}O and ^{40}Ca at $\hbar\omega = 22$ MeV and omit the Coulomb term in Eq. (51). This yields $a_V = 13.5$ MeV and $a_S = 11.5$ MeV, closer to the empirical values of $a_v \approx 16$ MeV and $a_S \approx 18$ MeV.

Let us again discuss uncertainties. We adopt the estimates made in light nuclei to the present case. Thus, the uncertainty from the EFT interaction is about 10% at NLO, implying $\Delta E_{\rm NLO}(^{16}{\rm O}) \sim 15$ MeV and $\Delta E_{\rm NLO}(^{40}{\rm Ca}) \sim 40$ MeV. The variation of binding energies with UV cutoff at fixed N and N_3 is in this range, and so are the uncertainties from the N_3 convergence of coupled cluster results at fixed Λ.

B. Lattice nuclei

We recompute ^{4}He with the coupled-cluster method and at NLO we find binding energies $E = 98.0$, 89.0, and 88.1 MeV for the interactions with $\hbar\omega = 5$, 10, and 22 MeV, respectively. This is in agreement with the NCSM results of Table IX and suggests that the normal-ordered two-body approximation of the *NNN* potential is accurate also for lattice nuclei. Again we find only a small amount of about 10% for the correlation energy. The small differences of about 1% between CCSD and NCSM results is due to neglected triples excitations.

TABLE XI. Binding energies of the lattice nuclei ^{16}O, ^{40}Ca for model space truncations as indicated, as a function of the cutoff Λ (or the oscillator spacing $\hbar\omega$). All quantities in units of MeV.

$\hbar\omega$	Λ	^{16}O		^{40}Ca	
		$N_1, N_3 = 12$	$N_1, N_3 = 14$	$N_1, N_3 = 12$	$N_1, N_3 = 14$
22	642.96	429.5	429.5	1187.0	1168.5
40	866.97	547.8	546.0	1252.0	1422.0

In contrast, at $\hbar\omega = 40$ MeV we find a ^{4}He binding energy of 99.5 MeV, which differs from the NCSM result by about 10%. Closer inspection and varying the strength of the *NNN* interaction suggests that this discrepancy is due to the normal-ordering two-body approximation of the *NNN* interaction at this frequency. As the normal-ordered two-body approximation is expected to improve with increasing mass number [102], we will also compute ^{16}O and ^{40}Ca at $\hbar\omega =$ 40 MeV, keeping in mind a conservative 10% uncertainty due to the normal ordering approximation.

Our results for ^{16}O and ^{40}Ca are shown in Table XI. We observe that lattice nuclei are bound with approximately 30 MeV per nucleon at $\hbar\omega = 22$ MeV. In a free Fermi gas this corresponds to a Fermi momentum $p_F \approx 310$ MeV. This is well below the pion mass employed in the lattice QCD calculations and also below the corresponding cutoff $\Lambda =$ 642.96 MeV of the EFT. For the smaller oscillator spacings $\hbar\omega = 5$ (corresponding to a cutoff of $\Lambda \approx 307$ MeV), we find binding energies per nucleon of about 37 MeV for ^{16}O and of about 50 MeV for ^{40}Ca. The corresponding Fermi momenta are about 340 and 400 MeV, clearly exceeding the cutoff. Thus, these calculations are not consistent with the underlying EFT assumptions. For the oscillator spacing $\hbar\omega = 10$ MeV, i.e., for $\Lambda \approx 433$ MeV, we find binding energies of about 23 and 22 MeV per nucleon for ^{16}O and ^{40}Ca, respectively. The corresponding Fermi momenta are about 270 MeV.

As for the light lattice nuclei, the error in the binding energy at NLO for lattice nuclei is of the order of 15% which leads to $\Delta E_{\rm NLO}(^{16}{\rm O}) \approx 75$ MeV and $\Delta E_{\rm NLO}(^{40}{\rm Ca}) \approx$ 200 MeV for ^{16}O and ^{40}Ca lattice nuclei. We remind the reader that this estimate excludes the dominant uncertainties due to the limited precision of the lattice QCD results that are input. At $\hbar\omega = 40$ MeV there also is an additional 10% uncertainty estimate due to the normal ordering approximation of *NNN* forces.

We return to the Bethe-Weizsäcker formula (51) for lattice nuclei, again omit the Coulomb term, and fit the volume and surface terms to ^{16}O and ^{40}Ca using the results at $\hbar\omega = 22$ and 40 MeV. This yields $a_V \approx 35$ to 40 MeV and $a_S \approx$ 14 to 22 MeV.

V. SUMMARY

We implemented pion-less EFT as a DVR in the harmonic oscillator basis. The DVR formulation has several advantages over traditional approaches that transform momentum-space interactions to the oscillator basis: (i) The UV cutoff and regulator are tailored to the underlying basis; (ii) the DVR facilitates the computation of matrix elements as this becomes essentially a function call; (iii) the IR improvement allows one to optimize interactions directly in the harmonic oscillator basis. We showed that the DVR formulation indeed yields an EFT with the correct low-momentum behavior.

To put the DVR in the context of momentum-space EFTs, we performed many checks and tests, and reported them in a set of appendixes. The Thomas effect [104] and the Tjon line [105] can be understood analytically from scaling arguments that connect the potential matrix elements at different UV cutoffs. Different implementations of the EFT—at constant UV cutof—yield results that differ by small amounts, consistent with expectations regarding regulator dependencies.

We calibrated the pion-less EFT for atomic nuclei and for lattice nuclei (at an unphysical pion mass) in $A = 2, 3$ systems and make predictions for ^{4}He, ^{16}O, and ^{40}Ca. At LO ^{16}O and ^{40}Ca are not bound with respect to decay into α particles; this deficiency is remedied at next-to-leading order. Varying the UV cutoff by about a factor of 2 suggests that pion-less EFT at next-to-leading order yields meaningful results for the binding energies of medium-mass nuclei that are consistent with chiral EFT calculations at that order.

Our results also suggest that medium-mass nuclei can be connected to lattice QCD input. Further progress in this direction, however, requires a resolution of the controversy between the different lattice QCD approaches to light nuclei, increasing the precision of the lattice QCD results that are input to EFTs, and finally, moving towards the physical pion mass.

ACKNOWLEDGMENTS

We thank B. Acharya, D. Furnstahl, L. Platter, and G. Rupak for useful discussions. We also thank B. van Kolck, D. Phillips, and I. Stetcu for questions and discussions during the program INT 17-1a "Toward Predictive Theories of Nuclear Reactions Across the Isotopic Chart," and D. Phillips for several useful communications. This material is based upon work supported in part by the US Department of Energy, Office of Science, Office of Nuclear Physics, under Awards No. DE-FG02-96ER40963 (University of Tennessee), No. DE-SC0008499, No. DE-SC0018223 (SciDAC NUCLEI Collaboration), the Field Work Proposal ERKBP57 at Oak Ridge National Laboratory (ORNL), the Leadership Computing Facility at ORNL under Contract No. DEAC05-00OR22725 (ORNL), Swedish Research Council under Grant No. 2015-00225, and Marie Sklodowska Curie Actions, Cofund Project No. INCA 600398. S.B. gratefully acknowledges the financial support from the Alexander-von-Humboldt Foundation (Feodor-Lynen fellowship).

This manuscript has been authored by UT-Battelle, LLC under Contract No. DE-AC05-00OR22725 with the US Department of Energy. The United States Government retains and the publisher, by accepting the article for publication, acknowledges that the United States Government retains a nonexclusive, paid-up, irrevocable, world-wide license to publish or reproduce the published form of this manuscript, or allow others to do so, for United States Government purposes.

The Department of Energy will provide public access to these results of federally sponsored research in accordance with the DOE Public Access Plan. (http://energy.gov/downloads/doe-public-access-plan).

APPENDIX A: OVERVIEW OF APPENDIXES

The formulation of pion-less EFT as a DVR in the oscillator basis invites questions regarding details of the implementation and its relation to established results. In these appendixes, we address a few relevant points. In Appendix B we show that a continuous family of DVR formulations exists, including one that exhibits a zero-momentum point. In Appendix C we show that the IR improvement of the LO two-body contact exhibits effective-range corrections that are parametrically small and inverse proportional to the number of DVR states. In Appendix D we derive simple scaling laws that govern the potential matrix elements as the oscillator frequency or the nucleon mass is varied. This makes it particularly simple to relate matrix elements corresponding to different UV cutoffs and to different nucleon masses. It also allows us to derive known relations such as the Thomas effect [104] or the Tjon [105] correlations. In Appendix E we confirm that our formulation of pion-less EFT obeys the Wigner bound [106]. In Appendix F we study the regulator dependence of our EFT by comparing different combinations of $(N, \hbar\omega)$ that yield similar UV cutoffs. In Appendix G we discuss the effects of oscillator basis truncation on *NNN* contact with cutoff in Jacobi momenta. Finally, Appendix H is dedicated to IR extrapolations. There, we show that Lüscher-like [80] formulas account for finite-size corrections that stem from finite harmonic oscillator spaces

APPENDIX B: DVR WITH A ZERO-MOMENTUM POINT

A discrete variable representation (DVR) in momentum space consists of basis functions $\tilde{\phi}_{\mu,l}(k)$ that are orthogonal to each other and localized around certain discrete momentum points. Let us start by expressing the DVR basis in terms of oscillator wave functions,

$$\tilde{\phi}_{\kappa,l}(k) = d_{\kappa,l} \sum_{n=0}^{N_l} \tilde{\psi}_{n,l}(\kappa)\tilde{\psi}_{n,l}(k). \tag{B1}$$

Here κ is a discrete momentum (to be determined) and $d_{\kappa,l}$ is a normalization constant. The DVR wave function $\tilde{\phi_{\kappa,l}}$ is the projection of a spherical wave with momentum κ onto the finite harmonic oscillator basis. To see this, we start from the completeness relation

$$\sum_{n=0}^{\infty} \tilde{\psi}_{n,l}(\kappa)\tilde{\psi}_{n,l}(k) = \frac{\delta(k-\kappa)}{k\kappa}, \tag{B2}$$

and note that this is also the orthogonality condition for spherical waves with momenta k and κ, respectively.

We need to determine the DVR points $\kappa = \kappa_\mu$ in the wave function (B1) such that wave functions belonging to different κ_μ are orthogonal to each other. Here μ enumerates the discrete set of momenta (the DVR points). The overlap between two such wave functions is

$$\begin{aligned}
&\int_0^\infty dk k^2 \tilde{\phi}_{\kappa_\mu,l}(k)\tilde{\phi}_{\kappa_\nu,l}(k) \\
&= d_{\kappa_\mu,l} d_{\kappa_\nu,l} \sum_{n=0}^{N_l} \tilde{\psi}_{n,l}(\kappa_\mu)\tilde{\psi}_{n,l}(\kappa_\nu) \\
&= d_{\kappa_\mu,l} d_{\kappa_\nu,l} \sqrt{(N_l+1)(N_l+l+3/2)} \\
&\quad \times \frac{\tilde{\psi}_{N_l,l}(\kappa_\mu)\tilde{\psi}_{N_l+1,l}(\kappa_\nu) - \tilde{\psi}_{N_l+1,l}(\kappa_\mu)\tilde{\psi}_{N_l,l}(\kappa_\nu)}{b^2\left(\kappa_\mu^2 - \kappa_\nu^2\right)}.
\end{aligned} \tag{B3}$$

For $\kappa_\mu \neq \kappa_\nu$, orthogonality implies

$$\frac{\tilde{\psi}_{N_l+1,l}(\kappa_\mu)}{\tilde{\psi}_{N_l,l}(\kappa_\mu)} = \frac{\tilde{\psi}_{N_l+1,l}(\kappa_\nu)}{\tilde{\psi}_{N_l,l}(\kappa_\nu)}, \tag{B4}$$

and we can solve for DVR points κ_μ by demanding that

$$\frac{\tilde{\psi}_{N_l+1,l}(\kappa_\mu)}{\tilde{\psi}_{N_l,l}(\kappa_\mu)} = R, \tag{B5}$$

with R being a constant.

Figure 12 shows the ratio in Eq. (B5) as a a function of momentum (red curve) for a model space with $N = 8$ and $l = 0$. The dashed-dotted horizontal line $R = 0$ yields the blue circles as intersection points; these are the DVR points we employed in the main text of this paper. The dashed horizontal line

$$R = \frac{\tilde{\psi}_{N_l+1,l}(0)}{\tilde{\psi}_{N_l,l}(0)} = \sqrt{\frac{N_l+l+3/2}{N_l+1}} \tag{B6}$$

yields the black triangles as intersection points. This is the DVR we seek as it contains the point $k = 0$. We note that there is a continuous set of DVRs, each being identified by the value of R.

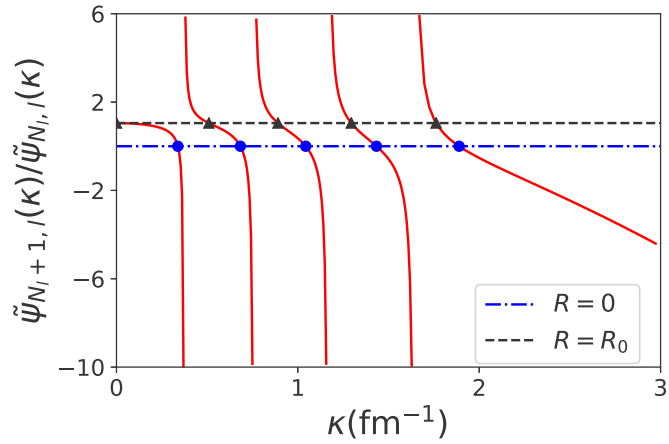

FIG. 12. Solid red curve: The ratio R of Eq. (B5) as a function of the momentum in a model space $N = 8$, $\hbar\omega = 22$ MeV, and $l = 0$. The dashed-dotted horizontal line corresponds to $R = 0$, and its intersection with the red curve, denoted by solid blue dots, yields the DVR points we used in the main text. The dashed line corresponds to the ratio $R = R_0$ in Eq. (B6), and the intersection of this line with red curve, denoted by solid black triangles, marks the DVR points of the DVR discussed in this Appendix.

To find the DVR points κ_μ, we solve

$$0 = \sqrt{\frac{N_l + l + 3/2}{N_l + 1}}\tilde{\psi}_{N_l,l}(\kappa) - \tilde{\psi}_{N_l+1,l}(\kappa), \tag{B7}$$

which is equivalent to

$$\begin{aligned} 0 &= (N + l + 3/2)L_{N_l}^{l+1/2}(\kappa^2 b^2) - (N_l + 1)L_{N_l+1}^{l+1/2}(\kappa^2 b^2) \\ &= \kappa^2 b^2 L_{N_l}^{l+3/2}(\kappa^2 b^2). \end{aligned} \tag{B8}$$

In the last step we used formula 8.971(4) of Ref. [107]. Thus, the DVR points are $\kappa = 0$ and the N_l roots of the polynomial $L_{N_l}^{l+3/2}(\kappa^2 b^2)$. It is understood that discrete momentum points are different for each partial wave and to keep our notation simpler we denote them by κ_μ instead of $\kappa_{\mu,l}$.

We note that Eq. (B5) only exhibits N_l solutions for $R > \tilde{\psi}_{N_l+1,l}(0)/\tilde{\psi}_{N_l,l}(0)$. For $R \to +\infty$, for instance, the solutions are N_l zeros of the generalized Laguerre polynomial $L_{N_l}^{l+1/2}(\kappa^2 b^2)$. This yields only N_l DVR functions. The remaining basis function is $\tilde{\psi}_{N_l+1,l}(k)$, but the resulting set of $N_l + 1$ basis functions is no longer a DVR.

We return to Eq. (B4) and compute the normalization for DVR wave functions whose momenta fulfill Eq. (B8). This yields

$$\begin{aligned} d_{\kappa_\mu,l}^{-2} &= -\sqrt{N_l(N_l+1)(N_l+l+3/2)} \\ &\quad \times \frac{\tilde{\psi}_{N_l-1,l+1}(\kappa_\mu)\tilde{\psi}_{N_l+1,l}(\kappa_\mu)}{\kappa_\mu b} \\ &= (N_l + l + 3/2)\left[\tilde{\psi}_{N_l,l}(\kappa_\mu)\right]^2 \\ &= (N_l + 1)\left[\tilde{\psi}_{N_l+1,l}(\kappa_\mu)\right]^2. \end{aligned} \tag{B9}$$

To derive this result, we employ the rule of l'Hospital, Eq. 8.971(2) from Ref. [107], and the recurrence relations between Laguerre polynomials. Returning to Eq. (B1) we compute

$$\tilde{\phi}_{\kappa_\mu,l}(k) = \frac{k}{b\left(k^2 - \kappa_\mu^2\right)}\tilde{\psi}_{N,l+1}(k). \tag{B10}$$

We note that the norm $d_{0,l}$ diverges as $(kb)^l$ for $\kappa = 0$ and $l > 0$. The corresponding localized eigenfunction in Eq. (B1) remains finite because $\tilde{\psi}_{n,l}(0) \propto (kb)^l$ and we have

$$\begin{aligned} \tilde{\phi}_{0,l}(k) &= \sqrt{\frac{N_l!\Gamma(l+5/2)}{\Gamma(N_l+l+5/2)\Gamma(l+3/2)}} \\ &\quad \times \sum_{n=0}^{N_l}\sqrt{\frac{\Gamma(n+l+3/2)}{n!}}\tilde{\psi}_{n,l}(k^2b^2). \end{aligned} \tag{B11}$$

We want to compare the DVR of this appendix to the one we used in the main text of the paper. In the large N_0 limit, the $(l = 0)$ wave functions of the latter DVR are essentially $j_0(k_{\mu,0}r)$ with $k_{\mu,0} \approx \mu\pi/L$. In contrast, the DVR points κ_μ of the DVR developed in this appendix which explicitly include $k = 0$ momentum satisfy $\kappa_\mu \approx (2\mu + 1)\pi/(2L)$, i.e., the DVR wave functions approach a Neumann boundary condition close to $r = L$. For other values of the ratio R of Eq. (B6), one obtains mixed boundary conditions close to $r = L$.

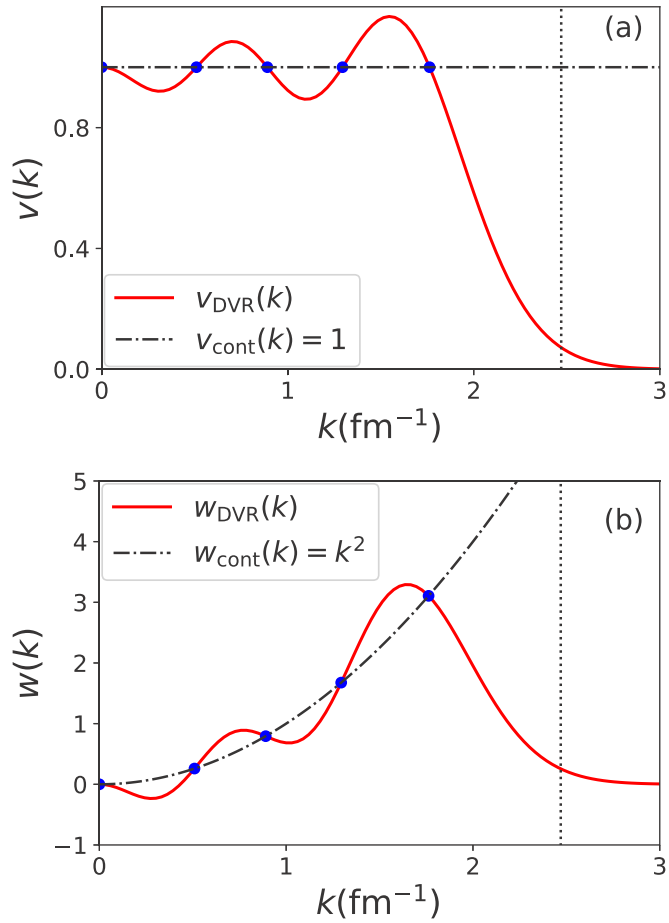

FIG. 13. The red curve shows the contact realized in a DVR with a zero-momentum point, in comparison with the original momentum-space contact shown as a dashed-dotted black line. The solid dots represent the DVR momenta. Note that $k = 0$ is a DVR point. Panel (a) [panel (b)] is for *NN* LO (NLO) interaction in pion-less EFT. The vertical black dotted line depicts the UV cutoff introduced by finite harmonic oscillator basis space with $l = 0$, $N = 8$, and $\hbar\omega = 22$ MeV.

Let us compute the S-wave *NN* contacts $v(k) = 1$ at LO and $w(k) = k^2$ at NLO in this DVR. The results are shown as solid red lines in Figs. 13(a) and 13(b), respectively. The original momentum-space interaction is plotted as a black dashed-dotted line. Dots represent the new discrete momenta, now including $k = 0$. The model-space parameters are $N = 8$ and $\hbar\omega = 22$ MeV.

While these DVR potentials are slightly more oscillatory than the IR-improved DVR potential in Figs. 2 and 4, they reproduce the original momentum-space interaction much better than the other DVR without IR improvement (red dashed curves in Figs. 2 and 4).

This makes it interesting to compute phase shifts with the DVR of this Appendix. Figure 14 shows the LO and NLO *np* phase shifts from the DVR interaction in $^1S_0$ [panel (a)] and $^3S_1$ [panel (b)] partial wave channels. Since at NLO *NN*

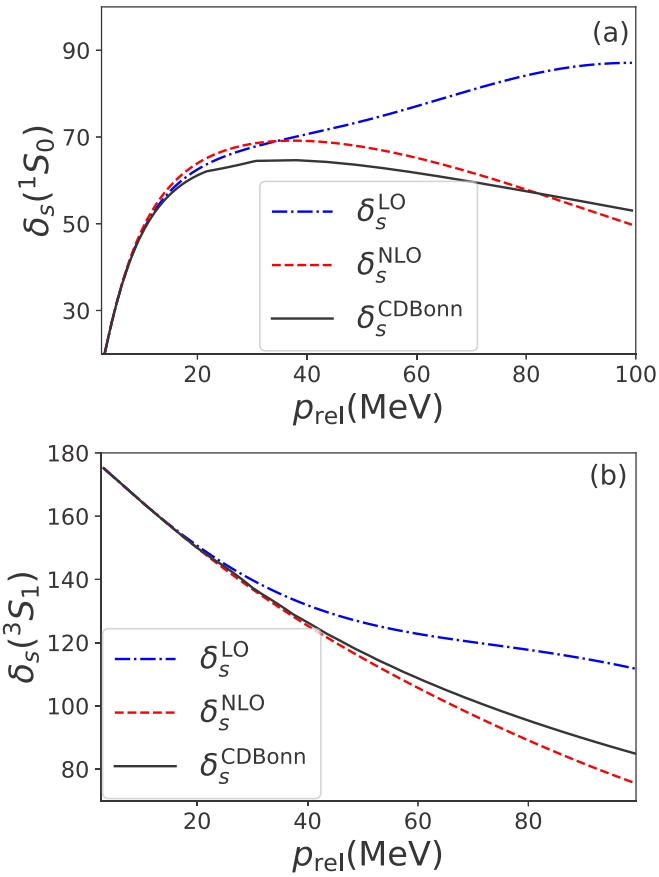

FIG. 14. The $^1S_0$ (a) and $^3S_1$ phase shifts (b) from a DVR potential at NLO (LO) in pion-less EFT in a model space $N = 8$, $\hbar\omega = 22$ MeV at NLO (red dashed line) and LO (blue dot-dashed line). The black curve shows the neutron-proton phase shifts of the CD-Bonn potential.

interaction in the DVR representation has incorrect curvature at $k = 0$, the NLO phase shifts are slightly oscillatory in both channels in comparison to phase shifts from IR improved interaction in the other DVR. Even so, we find it to be a simple alternative to the IR improvement.

APPENDIX C: IR IMPROVEMENTS AND EFFECTIVE RANGE

We want to understand the quality of the IR improvement of the *NN* contact. As the number of DVR states N_0 is finite, we have to understand finite-size effects. Here, we focus on the curvature of the function (25) at $k = 0$, as this introduces a finite range correction. To understand the finite size effects, we recall that—at low momenta and long wavelengths—the spherical harmonic oscillator basis is indistinguishable from a spherical cavity with radius $L = \pi/k_{0,0}$. This allows us to understand finite-size effects in the oscillator DVR by studying corresponding effects in a spherical cavity.

We therefore consider a spherical cavity of radius L. Eigenfunctions for S waves with momentum k_μ are spherical Bessel functions $j_0(\kappa r)$. In momentum space, the corresponding wave function results from a Fourier-Bessel transform,

$$\tilde{\psi}_\kappa(k) \equiv \frac{2}{\pi}\int_0^L dr r^2 j_0(\kappa r) j_0(kr) = \frac{1}{\pi\kappa k}\left(\frac{\sin(k-\kappa)L}{k-\kappa} - \frac{\sin(k+\kappa)L}{k+\kappa}\right). \quad \text{(C1)}$$

The momentum-space function $\tilde{\psi}_\kappa(k)$ is a smeared Dirac-δ function with a peak at $k = \kappa$ and also exhibits oscillations. As a check, we see that $\tilde{\psi}_\kappa(k) \to \delta(k-\kappa)/(\kappa k)$ for $L \to \infty$. The expression (C1) can be simplified when it is evaluated at the quantized momenta of

$$k_\mu \equiv \frac{\mu\pi}{L}. \quad \text{(C2)}$$

Then we have

$$\tilde{\psi}_{k_\mu}(k) = \frac{2L(-1)^\mu}{\pi}\frac{j_0(kL)}{k^2 - k_\mu^2}. \quad \text{(C3)}$$

In particular, the DVR property is

$$\tilde{\psi}_{k_\mu}(k_\nu) = \delta_\mu^\nu c_\mu^{-1} \quad \text{(C4)}$$

with

$$c_\mu^{-1} \equiv \frac{L^3}{\pi^3\mu^2}. \quad \text{(C5)}$$

To see the analogy with the oscillator DVR, we note that $\tilde{\psi}_{k_\mu}(k) \leftrightarrow \tilde{\psi}_{\mu,0}(k)$, and that $c_\mu \leftrightarrow c_{\mu,0}$. In an EFT based on N spherical Bessel functions, we would approximate the contact function $v_{\rm DVR}(k)$ of Eq. (23) as

$$\tilde{v}(k) \approx \sum_{\mu=1}^{N} c_\mu \tilde{\psi}_{k_\mu}(k). \quad \text{(C6)}$$

Here, the tilde indicates that this function exhibits oscillations. By construction, $\tilde{v}(k_\mu) = 1$, but this function is certainly not a constant. It has an oscillatory component, and at zero momentum we have

$$\tilde{v}(0) = \begin{cases} 2 & \text{for } N \text{ odd}, \\ 0 & \text{for } N \text{ even}. \end{cases} \quad \text{(C7)}$$

This suggests to make an IR improvement by adding one more basis function with momentum k_{N+1}, and with half the usual amplitude. (Alternatively, we could reduce the amplitude at k_N by a factor 2 as is approximately done for the oscillator DVR; see Fig. 2.) This yields

$$\bar{v}(k) = \sum_{\mu=1}^{N} c_\mu \tilde{\psi}_{k_\mu}(k) + \frac{c_{N+1}}{2}\tilde{\psi}_{k_{N+1}}(k) = 2j_0(kL)\sum_{\mu=1}^{N}\frac{(-1)^\mu\mu^2}{\left(\frac{kL}{\pi}\right)^2 - \mu^2} + j_0(kL)\frac{(-1)^{N+1}(N+1)^2}{\left(\frac{kL}{\pi}\right)^2 - (N+1)^2}. \quad \text{(C8)}$$

By construction, $\bar{v}(k_\mu) = 1$ for $\mu = 1, \ldots, N$ and $\bar{v}(0) = 1$. The function $\bar{v}$ exhibits oscillations with a much reduced amplitude in comparison to $\tilde{v}$, and it is an even function in

k. To gauge its quality in the IR, we compute its curvature at $k = 0$. For $k \to 0$ we find

$$\overline{v}(k) \approx 1 - \frac{k^2 L^2}{\pi^2}\left[\frac{\pi^2}{6} + 2\sum_{\mu=1}^{N}\frac{(-1)^\mu}{\mu^2} - \frac{(-1)^N}{(N+1)^2}\right]. \tag{C9}$$

We use

$$\sum_{n=1}^{K}\frac{(-1)^n}{n^2} = \frac{1}{2}\sum_{n=1}^{[K/2]}\frac{1}{n^2} - \sum_{n=1}^{K}\frac{1}{n^2}. \tag{C10}$$

Here, $[x]$ denotes the integer part of x. We rewrite

$$\sum_{n=1}^{K}\frac{1}{n^2} = \sum_{n=1}^{\infty}\frac{1}{n^2} - \sum_{n=K+1}^{\infty}\frac{1}{n^2} = \frac{\pi^2}{6} - \sum_{n=K+1}^{\infty}\frac{1}{n^2}, \tag{C11}$$

and employ the Euler-Maclaurin summation formula

$$\sum_{n=K+1}^{\infty}\frac{1}{n^2} = \frac{1}{K} - \frac{1}{2K^2} + \mathcal{O}(K^{-3}). \tag{C12}$$

Thus, the expansion (C9) becomes

$$\overline{v}(k) \approx 1 + \mathcal{O}\left(\frac{(kL)^2}{N^3}\right). \tag{C13}$$

This result is also confirmed numerically. Using $L\Lambda \propto N$, we see that the quadratic correction scales as

$$\frac{1}{N}\left(\frac{k}{\Lambda}\right)^2. \tag{C14}$$

Thus, the effective range correction of the IR-improved contact is parametrically small as the number N of DVR points increases. This is an interesting and encouraging result. The IR improved contact in an EFT based on the lowest N discrete momentum states of a spherical cavity exhibits small effective-range corrections proportional to $1/N$. This correction vanishes as $N \to \infty$ and is clearly a finite-size effect.

We also note here that the IR improvement of the contact essentially reduces the weight of the eigenfunction corresponding to the largest momentum by a factor of about 0.5. This suggests a simple way to perform IR improvements. In the partial wave with angular momentum l we introduce nonlocal regulators for the potential via

$$V(p', l'; p, l) \to e^{-(p'/k_{N_{l'},l'})^{2n}} V(p', l'; p, l) e^{-(p/k_{N_l,l})^{2n}}.$$

This widely used regulator approximately introduces the factor $1/2$ reduction at about the right momentum. In practice we find that this simple procedure works quite well, in particular for chiral interactions where analytical IR improvements might be more tedious.

APPENDIX D: THOMAS EFFECT AND TJON LINE

In this Appendix, we derive simple scaling relations that hold at fixed N. We will use them to explain the key results the Thomas effect [104] (i.e., the increase of binding in the three-nucleon system with increasing cutoff of the *NN* interaction) and the Tjon line [105] (i.e., the correlation between binding energies of the $A = 3$ and $A = 4$ bound states). These results suggest that the EFT as a DVR in the oscillator basis is also useful to obtain analytical insights.

In what follows we vary the UV cutoff (7) at fixed number of oscillator shells N by changing the oscillator length b, i.e., the oscillator frequency $\hbar\omega$. We also allow the nucleon mass to vary, as this will be useful with view on lattice nuclei. As we will see, varying $\hbar\omega$ or nucleon mass m simply rescales the matrix elements of the contact interactions and kinetic energy in the oscillator EFT.

From Eqs. (14) and (9) we find $\tilde{\psi}_{n,l}(k) \propto b^{3/2}$, $c_{\mu,l} \propto b^{-3/2}$, and $k_{\mu,l} \propto b^{-1}$. Thus, the roots of the generalized Laguerre polynomial $L_{N+1}^{l+1/2}(k^2b^2)$ do not change, and a rescaling of b and m simply changes the matrix elements of the LO contact, the NLO contact, and the three-nucleon force as

$$\begin{aligned} V_{\rm LO} &\propto C_{\rm LO} b^{-3} \propto C_{\rm LO}(m\hbar\omega)^{3/2}, \\ V_{\rm NLO} &\propto C_{\rm NLO} b^{-5} \propto C_{\rm NLO}(m\hbar\omega)^{5/2}, \\ V_{NNN} &\propto C_{NNN} b^{-6} \propto C_{NNN}(m\hbar\omega)^{3}, \end{aligned} \tag{D1}$$

respectively. The Schrödinger equation for two nucleons at leading order in either the ${}^1S_0$ or the ${}^3S_1$ partial wave is

$$\frac{\hbar^2}{mb^2}\left(\hat{t}_2 + m\hbar\frac{C_{\rm LO}}{b}\hat{v}_2\right)|\psi\rangle = E_2|\psi\rangle. \tag{D2}$$

Here, $\hat{t}_2$ and $\hat{v}_2$ are dimensionless matrices of the kinetic and potential energies, respectively. Thus,

$$\left(\hat{t}_2 + m\hbar\frac{C_{\rm LO}}{b}\hat{v}_2\right)|\psi\rangle = \frac{E_2}{\hbar\omega}|\psi\rangle \approx 0. \tag{D3}$$

The last approximation is exact in the case of an infinite scattering length or a zero-energy bound state. It is a good approximation in general as most model spaces of *ab initio* calculations have $E_2/(\hbar\omega) \ll 1$. Thus,

$$\frac{C_{\rm LO}}{b} m\hbar = \text{const}. \tag{D4}$$

This relation implies $C_{\rm LO} \propto (\hbar\omega)^{-1/2}$ and is the oscillator-EFT equivalent of the well-known relation $C_{\rm LO} \propto (m\Lambda)^{-1}$ in the momentum-space formulation of pion-less EFT at infinite scattering length (or zero-energy bound states).

Let us now consider the Schrödinger equation for the A-body system, based on *NN* interactions at LO. We find similar to Eq. (D2) that

$$E_A|\psi\rangle = \frac{\hbar^2}{mb^2}\left(\hat{t}_A + m\hbar\frac{C_{\rm LO}}{b}\hat{v}_A\right)|\psi\rangle = \frac{\hbar^2}{mb^2}\hat{h}_A|\psi\rangle. \tag{D5}$$

Here, $\hat{t}_A$, and $\hat{v}_A$ are the dimensionless matrices for the kinetic and potential energy in the A-body system, respectively. These quantities do not depend on the oscillator length. We note that $\hat{h}_A$ is a dimensionless matrix that is independent of b because of the scaling relation (D4). Thus,

$$E_A \propto \frac{\hbar^2}{mb^2} = \hbar\omega. \tag{D6}$$

This scaling relation explains the Thomas effect [104]: the binding energy of the $A = 3$ system increases with decreasing range of the potential, i.e., with increasing cutoff or increasing $\hbar\omega$. It also explains the Tjon line [105], i.e., the correlation

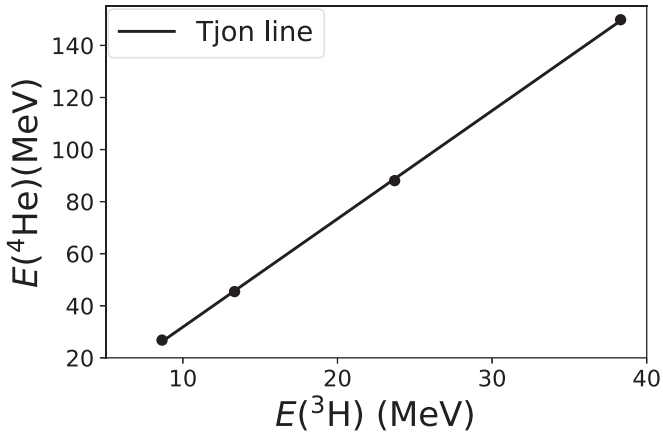

FIG. 15. Correlation between the triton and ^{4}He binding energies, computed in LO with *NN* interactions from pion-less EFT. Different points correspond to different UV cutoffs.

between the binding energies of the $A = 3$ and $A = 4$ nuclei. Of course, both effects led to beautiful insights regarding the renormalization of the $A = 3$ body system via a three-body force [66] and the Tjon line as a generic property of systems with large scattering lengths [13]. To illustrate our analytical insights we use the results obtained for *NN* potentials alone (see, e.g., Table III) and show the Tjon correlations, i.e., the proportionality of the binding energies for $A = 3$ nuclei and ^{4}He in Fig. 15.

APPENDIX E: LARGE UV CUTOFFS AND THE WIGNER BOUND

Based on the Wigner [106] bound on the derivative of phase shifts, Phillips and Cohen [108] showed that the effective range r_e of the potential obeys the inequality

$$r_e \leqslant 2\left(R - \frac{R^2}{a} + \frac{R^3}{3a^2}\right). \tag{E1}$$

Here, R is the physical range of the potential, i.e., the radius beyond which the potential is zero and a is the scattering length. As the physical range scales as $R \propto \Lambda^{-1}$ for interactions with a UV cutoff Λ, it is clear that the effective range expansion (3) cannot be reproduced at sufficiently large UV cutoffs. How does the EFT employed in this work reflect this behavior?

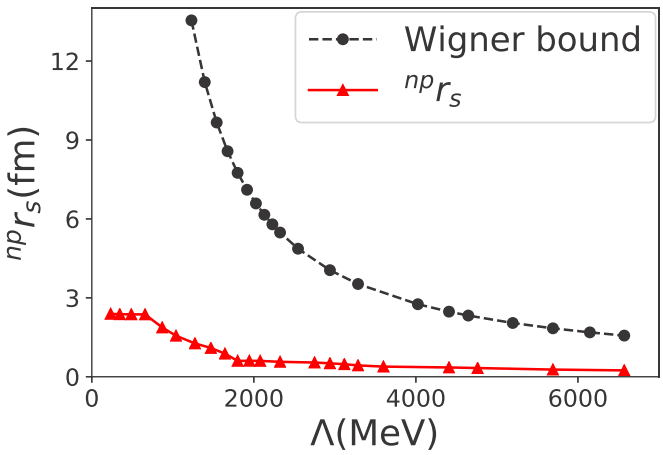

FIG. 16. The effective range in the singlet S wave (red line) as a function of the UV cutoff. The blue line shows the Wigner bound.

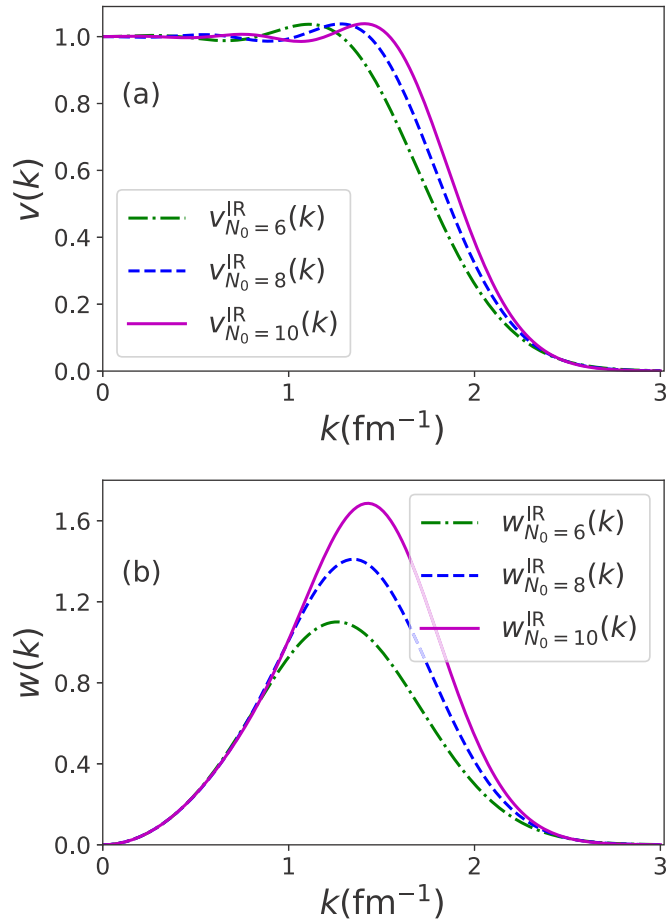

FIG. 17. The dash-dotted green (solid magenta) curve shows the *NN* interaction in model space $N = 6$, $\hbar\omega = 26.63$ MeV, ($N = 10$, $\hbar\omega = 18.74$ MeV). The dashed blue curve shows the same interactions in model space $N = 8$, $\hbar\omega = 22$ MeV. Panels (a) and (b) correspond to *NN* interaction at LO and NLO, respectively. All three cases have a momentum cutoff $\Lambda \approx 487$ MeV.

Figure 16 shows the effective range in the singlet S wave (red curve) obtained from a fit to the effective range expansion (3) for NLO interactions regularized in a finite harmonic oscillator basis with $N = 8$. The UV cutoff is increased by increasing the oscillator spacing $\hbar\omega$. For each cutoff, the LECs of the NLO potential are obtained from a χ^2-fit to low energy phase shifts, and the χ^2 objective function contains NLO uncertainty estimates. For cutoffs exceeding $\Lambda \approx 650$ MeV, we are unable to reproduce the effective range of the *NN* interaction. The dashed black curve shows the Wigner bound, i.e., the equality sign holds in Eq. (E1). We see that our EFT obeys the Wigner bound. We also note that the effective range seems to approach zero for very large cutoffs. Negative effective ranges (as discussed in Ref. [108]) are not realized in our EFT.

TABLE XII. The LECs of the *NN* potential at LO for physical nuclei at constant $\Lambda \approx 487$ MeV and varying model space size.

N	$\hbar\omega$	$\tilde{C}_{^3s_1}$	$\tilde{C}_{^1s_0}$
6	26.63	−0.407 880	−0.313 361
8	22	−0.379 465	−0.296 100
10	18.74	−0.360 988	−0.284 491

TABLE XIII. *NN* LECs at NLO for physical nuclei at constant $\Lambda \approx 487$ MeV and varying model space size.

N	$\hbar\omega$	$\tilde{C}_{^3s_1}$	$C_{^3s_1}$	$\tilde{C}_{^1s_0}$	$C_{^1s_0}$
6	26.63	−0.792 415	0.834 806	−0.571 535	0.469 715
8	22	−0.809 378	0.772 254	−0.612 966	0.691 221
10	17.84	−0.798 677	0.693 435	−0.587 451	0.614 043

APPENDIX F: REGULATOR EFFECTS

In the DVR implementation of pion-less EFT, the UV cutoff (7) can be varied at fixed N by changing the oscillator frequency $\hbar\omega$. Strictly speaking the variation of $\hbar\omega$ also changes the IR cutoff, but the IR improvement essentially eliminates the effect of this variation on the potential.

In this Appendix we will consider different combinations of $(N, \hbar\omega)$ that keep the UV cutoff constant and thus correspond to different regulators. In an EFT, regulator dependencies are expected to be higher-order effects. Thus, we expect that IR improved interactions with an identical UV cutoff but different $(N, \hbar\omega)$ combinations should yield similar results for finite nuclei. How small can N be chosen? Semiclassical arguments indicate that the number N should scale as $N \propto A^{1/3}$ so that all nucleons are indeed interacting. But besides this, there seems to be little to be gained by considering (unnecessary) large interaction spaces.

To probe regulator dependencies, we consider model spaces with combinations $N = 6$, $\hbar\omega = 26.63$ MeV, $N = 8$, $\hbar\omega = 22$ MeV, and $N = 10$, $\hbar\omega = 18.74$ MeV; these have a similar UV cutoff $\Lambda \approx 487$ MeV. Figure 17 shows that the IR-improved potentials $v(k) = 1$ at LO and $w(k) = k^2$ at NLO are similar for the different model spaces. Due to the IR improvement, the effective UV cutoff decreases somewhat with decreasing N, but the differences are small, particularly at low momenta. This suggests that the different model spaces translate into small differences in the effective regulator functions.

We fit the *NN* potential at LO to the scattering lengths and the deuteron binding energy. The resulting LECs are shown in Table XII. We note that the LECs exhibit only a small dependency on the model space, keeping up with EFT expectations that regulator dependencies at similar cutoffs are higher-order effects.

We turn to the *NN* interaction at NLO and employ the effective ranges as additional constraints to determine the LECs. Table XIII shows the results. Again we observe a mild dependence of the model space, and this is again consistent with EFT expectations that regulator dependencies are higher-order effects.

We turn to the *NNN* contact. Figure 18 compares *NNN* function $\bar{u}(k, p)$ regulated in hyper-radial momentum for three model spaces of interest. All three interactions are quite similar, particularly at low momenta. We note that this observation also extends to *NNN* contact when regulated in each Jacobi momentum.

We include the *NNN* contact and determine its LEC by adjusting to the triton binding energy. We perform two independent computations of the ground-state energies and matter radii of $A = 3, 4$ nuclei (at a physical pion mass) from these *NN* interactions at LO and NLO, and present the results in Table XIV.

We also performed calculations where the *NNN* interaction is regulated in each of the Jacobi momenta. Table XV shows the results. The comparison with Table XIV shows that regulator differences in the *NNN* contact are small, as expected in an EFT.

APPENDIX G: EFFECTS OF OSCILLATOR BASIS TRUNCATION ON *NNN* CONTACT

In this Appendix we discuss the effects of an oscillator basis truncation where the *NNN* interaction matrix elements of the oscillator states with $n_1 + n_2 > N_3$ are set to zero. Here and throughout this appendix, n_1 and n_2 are principal

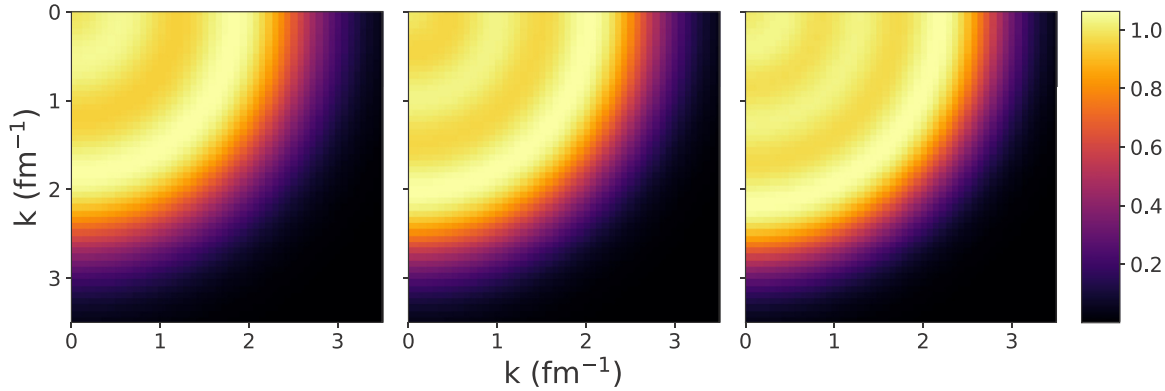

FIG. 18. Momentum space matrix elements $\bar{u}(k, p) = c_{\mu,0} c_{\nu,0} u^{\rm IR}_{\rm DVR}(\sqrt{k^2 + p^2})$ in harmonic oscillator basis with $N = 6$ (left), 8 (center), and 10 (right) with identical UV cutoff. The x and y axes represent Jacobi momenta in fm^{-1}.

TABLE XIV. Binding energies and radii for $A = 3, 4$ nuclei at constant $\Lambda \approx 487$ MeV and different model spaces employing a hyperspherical regulator for the *NNN* contact. The *NNN* coupling c_E is adjusted to reproduce the triton binding energy $B_t = 8.482$ MeV.

$E_{3\max} = N$ (triangular)						
LO						
N	c_E	$r(^3\mathrm{H})$	$E(^3\mathrm{He})$	$r(^3\mathrm{He})$	$E(^4\mathrm{He})$	$r(^4\mathrm{He})$
6	−0.269 308	1.30	7.55	1.47	18.28	1.45
8	−0.238 514	1.29	7.52	1.46	17.66	1.46
10	−0.218 702	1.28	7.50	1.45	17.27	1.46
NLO						
N	c_E	$r(^3\mathrm{H})$	$E(^3\mathrm{He})$	$r(^3\mathrm{He})$	$E(^4\mathrm{He})$	$r(^4\mathrm{He})$
6	−0.073 289	1.58	7.71	1.77	28.39	1.36
8	−0.008 170	1.63	7.77	1.83	29.30	1.44
10	−0.024 851	1.63	7.77	1.82	27.90	1.51

harmonic oscillator quantum numbers for a three-nucleon system in intrinsic Jacobi coordinates.

The *NNN* contact with the hyperspherical cutoff in Eq. (44) remains unaffected by this truncation for $N_3 \geqslant N$, because it fulfills $n_1 + n_2 \leqslant N$ by construction. This is the key reason why we chose to work with the hyperspherical regulator in this paper. On the other hand, the IR improved *NNN* interaction (34) with cutoff in Jacobi momenta is affected by this truncation once $N_3 < 2N$. As shown in Fig. 19, lowering N_3 below $2N = 16$ significantly modifies the *NNN* contact with cutoff in Jacobi momenta after truncation. Here, $N_3 = 6$, 8, and 10 are shown by the dash-dotted green, dashed blue, and solid magenta lines respectively.

Not surprisingly, in the truncated bases with $N_3 < 2N = 16$ the ground-state energy of ^{4}He exhibits a strong dependence on the N_3 truncation. In an effort to reduce the number of matrix elements of the *NNN* force, we also employed the *NNN* contact (34) such that the interaction vanishes for $n_1, n_2 > N/2$. (This would still keep *NNN* excitations up to $N\hbar\omega$ in the potential.) Choosing combinations of N and $\hbar\omega$ that exhibit similar UV cutoffs, we found that the ^{4}He binding energy increases with increasing N for this truncation.

TABLE XV. Same as Table XIV but for regulators in each Jacobi coordinate of the *NNN* force.

$E_{3\max} = 2N$ (square)						
LO						
N	c_E	$r(^3\mathrm{H})$	$E(^3\mathrm{He})$	$r(^3\mathrm{He})$	$E(^4\mathrm{He})$	$r(^4\mathrm{He})$
6	−0.224 040	1.33	7.58	1.49	21.28	1.51
8	−0.191 847	1.32	7.56	1.48	20.82	1.40
10	−0.171 713	1.31	7.55	1.47	23.07	1.38
NLO						
N	c_E	$r(^3\mathrm{H})$	$E(^3\mathrm{He})$	$r(^3\mathrm{He})$	$E(^4\mathrm{He})$	$r(^4\mathrm{He})$
6	−0.059 819	1.58	7.71	1.78	28.34	1.40
8	−0.006 553	1.68	7.77	1.83	29.27	1.45
10	−0.020 162	1.63	7.77	1.66	28.13	1.51

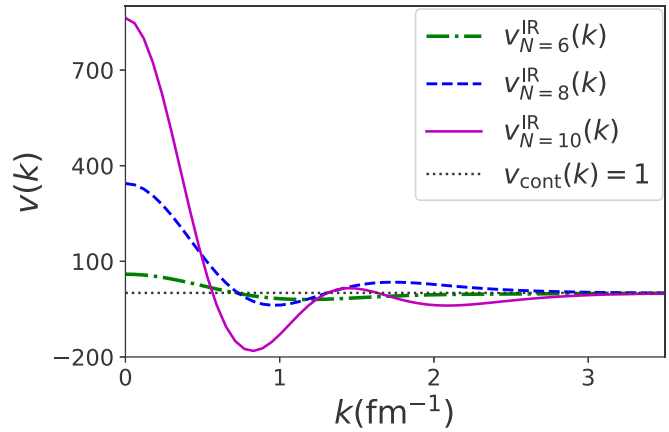

FIG. 19. The v_{DVR} of *NNN* interaction (34) reconstructed only from interaction matrix elements in remaining harmonic oscillator basis states after $n_1 + n_2 \leqslant N_3$ truncation. Dashed-dotted green line: *NNN* interaction in model space $N_3 = 6$ and $\hbar\omega = 26.63$ MeV; dashed blue line: $N_3 = 8$ and $\hbar\omega = 22$ MeV; solid magenta line: $N_3 = 10$ and $\hbar\omega = 18.74$ MeV. All three cases have the same momentum cutoff $\Lambda \approx 487$ MeV. The dotted black line shows the original momentum space interaction $v = 1$.

APPENDIX H: IR EXTRAPOLATIONS

The EFT formulation in the harmonic oscillator basis provides us with a UV cutoff that is tailored to the model space, and this makes UV extrapolations [77] unnecessary. To overcome finite-volume effects, one can employ IR extrapolations. The corresponding extrapolation [75] formulas generalize Lüscher's approach [80] to the harmonic oscillator.

The EFT potential is defined in a model space of size N. For the Hamiltonian matrix we choose $N_{\max} \geqslant N$ such that the potential is active only between states with energy $E \leqslant N\hbar\omega$, while the kinetic energy is active in the full space, i.e., in all states with energy $E \leqslant N_{\max}\hbar\omega$. (Here, we neglected the zero-point energy.) As $N_{\max}$ increases the radius L associated with the harmonic oscillator basis also increases, and the tail of the bound-state wave function becomes increasingly accurate. For energies, we have [75]

$$E(N_{\max}) = E_\infty + ae^{-2k_\infty L} \tag{H1}$$

as the leading correction for $k_\infty L \gg 1$. For the deuteron, k_∞ is the bound-state momentum [76] and L is calculated using the Eq. (6). In general, k_∞ is the separation momentum of the lowest breakup channel [86,87], i.e.,

$$S = \frac{\hbar^2 k_\infty^2}{2m} \tag{H2}$$

is the separation energy of the lowest-lying breakup channel. This suggests that the relevant small momentum scale k_{sep} might be much larger than the low-momentum scales encountered in the deuteron and in the effective range expansion of the nuclear force. A separation energy of 8 MeV, for instance, corresponds to a separation momentum of about 120 MeV.

Let us illustrate the extrapolation using the example of the deuteron at NLO and in a model space $N = 8$ for the potential. Figure 20 shows that the energy difference

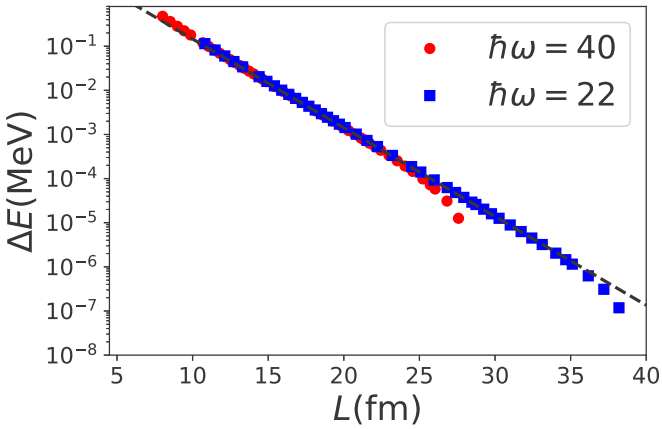

FIG. 20. Difference of the deuteron binding energy in a finite space of size L and the infinite-space result for $\hbar\omega = 40$ MeV (solid red dots) and 22 MeV (solid blue squares) for our NLO oscillator EFT potential in model space $N = 8$. The dashed black line shows $a\exp(-2k_\infty L)$ where $k_\infty \equiv 0.2316$ fm^{-1} is the separation momentum.

$\Delta E \equiv E(N_{\max}) - (E_\infty)_{\text{actual}}$ converges exponentially fast as a function of L. Solid red dots (solid blue squares) $\hbar\omega =$ 40 MeV (22 MeV), and the dashed black line is the function $a\exp(-2k_\infty L)$ with $a \approx 15$ MeV and the separation momentum 0.2316 fm^{-1}. We note that the exponential decay is indeed governed by the separation momentum and that the equality of this momentum and k_∞ is much more accurate here than reported in Ref. [76]. The reason is presumably the fully achieved UV convergence in the present approach.

Though the no-core shell-model calculations for $A = 3, 4$ nuclei are virtually converged with respect to the model space, it is still useful to consider IR extrapolation. At low energies, the harmonic oscillator is indistinguishable from a spherical cavity of radius L. For the no-core shell model, the radius L is a known function of the number of shells N and the frequency $\hbar\omega$ of the employed basis [79]. The NLO calculation of ^{3}H with an EFT potential of $N = 8$ and $\hbar\omega = 22$ MeV. As the formula (H1) depends on the three parameters (E_∞, k_∞, a), extrapolations start from three data points of the ground-state energy $E(L) = E(N_{\max})$ computed in $N_{\max} = 8, 10, 12$. Figure 21 compares $E(N_{\max})$ with the extrapolation result E_∞. From $N_{\max} = 14$ and higher, the extrapolated result is much more accurate than the finite-volume result.

For the triton, the lowest open decay channel is $t \to d + n$, with a separation momentum fulfilling

$$\frac{\hbar^2 k_{\text{sep}}^2}{2m} = B_t - B_d, \tag{H3}$$

where B_t and B_d are the binding energies of the triton and deuteron, respectively. Figure 22 compares the theoretical value of k_{sep}, computed from the theoretical energy differences, with the results k_∞ from the extrapolation. Both quantities become close, but not identical, as the model space is increased. We do not completely understand the reason for the difference between k_{sep} and k_∞. However, at LO and using NN forces only, the triton is strongly bound, and the agreement between k_∞ and k_{sep} is much better.

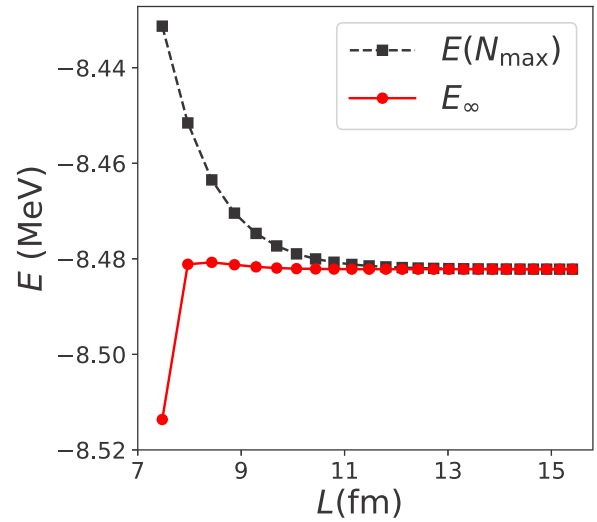

FIG. 21. Ground-state energy (black squares) of ^{3}H computed in a model space of $N_{\max} + 1$ shells and compared to the IR extrapolated result E_∞ (red circles).

We turn to ^{4}He, where the lowest-energetic breakup channel is $\alpha \to t + p$. We consider the case of the NLO calculation with a potential defined in $N = 8$ and $\hbar\omega = 40$ MeV. Figure 23 shows the convergence of the energy as the model space is increased and compares it to the extrapolated result.

For this case, we can also compare the value of the extrapolated momentum k_∞ with that of the corresponding separation momentum. The results are shown in Fig. 24. Here, the extrapolated k_∞ is somewhat smaller than the separation momentum k_{sep}, but the results are not yet converged as the model space is increased.

Overall, the results of this Appendix show that the IR extrapolations of the EFT realized as a DVR in the harmonic oscillator basis work quite well and agree with expectations.

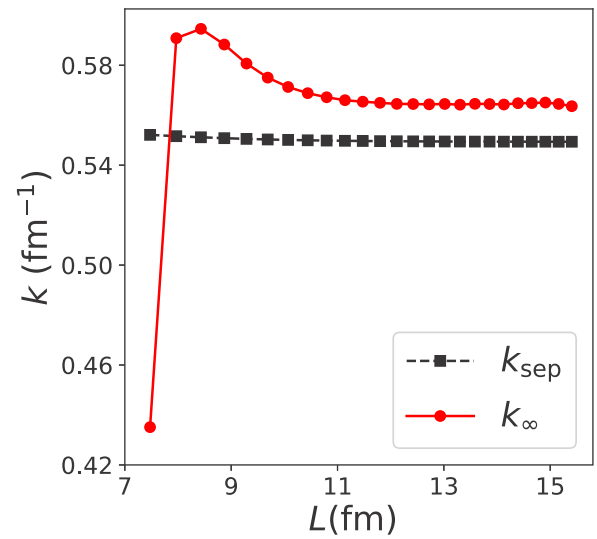

FIG. 22. Separation momentum (black squares) of ^{3}H computed in a model space of $N_{\max} + 1$ shells and compared to the IR extrapolated result k_∞ (red circles).

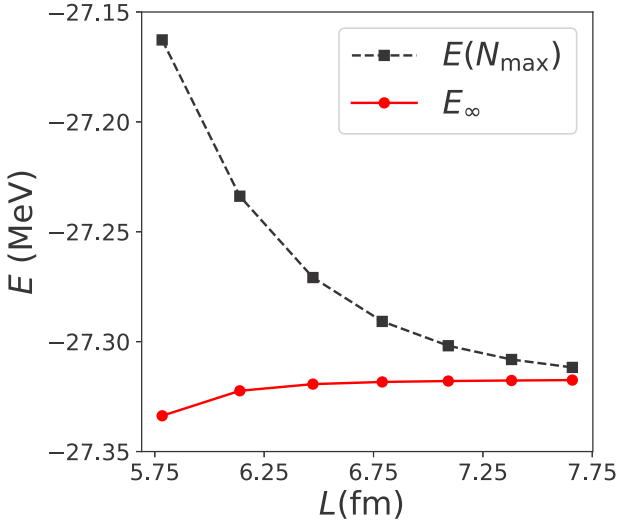

FIG. 23. Ground-state energy (black squares) of ^{4}He computed in a model space of $N_{max} + 1$ shells and compared to the IR extrapolated result E_∞ (red circles).

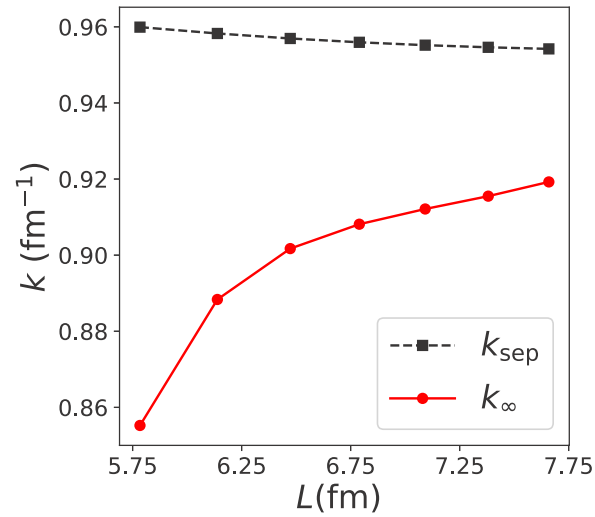

FIG. 24. Separation momentum (black squares) of ^{4}He computed in a model space of $N_{max} + 1$ shells and compared to the IR extrapolated result k_∞ (red circles).

[1] P. F. Bedaque and U. van Kolck, Effective field theory for few-nucleon systems, Annu. Rev. Nucl. Part. Sci. **52**, 339 (2002).

[2] H.-W. Hammer and L. Platter, Efimov states in nuclear and particle physics, Annu. Rev. Nucl. Part. Sci. **60**, 207 (2010).

[3] H. W. Grießhammer, J. A. McGovern, D. R. Phillips, and G. Feldman, Using effective field theory to analyze low-energy compton scattering data from protons and light nuclei, Prog. Part. Nucl. Phys. **67**, 841 (2012).

[4] S. König, H. W. Grießhammer, H.-W. Hammer, and U. van Kolck, Effective theory of 3h and 3he, J. Phys. G: Nucl. Part. Phys. **43**, 055106 (2016).

[5] C. A. Bertulani, H.-W. Hammer, and U. van Kolck, Effective field theory for halo nuclei: shallow p-wave states, Nucl. Phys. A **712**, 37 (2002).

[6] R. Higa, H.-W. Hammer, and U. van Kolck, $\alpha\alpha$ scattering in halo effective field theory, Nucl. Phys. A **809**, 171 (2008).

[7] H.-W. Hammer and D. R. Phillips, Electric properties of the beryllium-11 system in halo {EFT}, Nucl. Phys. A **865**, 17 (2011).

[8] E. Ryberg, C. Forssén, H.-W. Hammer, and L. Platter, Effective field theory for proton halo nuclei, Phys. Rev. C **89**, 014325 (2014).

[9] H.-W. Hammer and R. J. Furnstahl, Effective field theory for dilute fermi systems, Nucl. Phys. A **678**, 277 (2000).

[10] S. R. Beane, E. Chang, S. D. Cohen, W. Detmold, H. W. Lin, T. C. Luu, K. Orginos, A. Parreño, M. J. Savage, and A. Walker-Loud (NPLQCD Collaboration), Light nuclei and hypernuclei from quantum chromodynamics in the limit of su(3) flavor symmetry, Phys. Rev. D **87**, 034506 (2013).

[11] N. Barnea, L. Contessi, D. Gazit, F. Pederiva, and U. van Kolck, Effective Field Theory for Lattice Nuclei, Phys. Rev. Lett. **114**, 052501 (2015).

[12] L. Contessi, A. Lovato, F. Pederiva, A. Roggero, J. Kirscher, and U. van Kolck, Ground-state properties of ^{4}He and ^{16}O extrapolated from lattice QCD with pionless EFT, Phys. Lett. B **772**, 839 (2017).

[13] L. Platter, H.-W. Hammer, and U.-G. Meißner, On the correlation between the binding energies of the triton and the α-particle, Phys. Lett. B **607**, 254 (2005).

[14] J. Kirscher, H. W. Grießhammer, D. Shukla, and H. M. Hofmann, Universal correlations in pion-less eft with the resonating group method: Three and four nucleons, Eur. Phys. J. A **44**, 239 (2010).

[15] J. Kirscher, H. W. Griesshammer, D. Shukla, and H. M. Hofmann, Universal correlations in pion-less EFT with the resonating group model: three and four nucleons, PoS **CD09**, 105 (2009).

[16] J. Kirscher, Pionless Effective Field Theory in Few-Nucleon Systems, Ph.D. thesis, George Washington University, 2015.

[17] V. Lensky, M. C. Birse, and N. R. Walet, Description of light nuclei in pionless effective field theory using the stochastic variational method, Phys. Rev. C **94**, 034003 (2016).

[18] I. Stetcu, B. R. Barrett, and U. van Kolck, No-core shell model in an effective-field-theory framework, Phys. Lett. B **653**, 358 (2007).

[19] U. van Kolck, Few-nucleon forces from chiral Lagrangians, Phys. Rev. C **49**, 2932 (1994).

[20] E. Epelbaum, H.-W. Hammer, and U.-G. Meißner, Modern theory of nuclear forces, Rev. Mod. Phys. **81**, 1773 (2009).

[21] R. Machleidt and D. R. Entem, Chiral effective field theory and nuclear forces, Phys. Rep. **503**, 1 (2011).

[22] S. Binder, P. Piecuch, A. Calci, J. Langhammer, P. Navrátil, and R. Roth, Extension of coupled-cluster theory with a noniterative treatment of connected triply excited clusters to three-body hamiltonians, Phys. Rev. C **88**, 054319 (2013).

[23] T. A. Lähde, E. Epelbaum, H. Krebs, D. Lee, U.-G. Meißner, and G. Rupak, Lattice effective field theory for medium-mass nuclei, Phys. Lett. B **732**, 110 (2014).

[24] G. Hagen, T. Papenbrock, M. Hjorth-Jensen, and D. J. Dean, Coupled-cluster computations of atomic nuclei, Rep. Prog. Phys. **77**, 096302 (2014).

[25] G. Hagen, A. Ekström, C. Forssén, G. R. Jansen, W. Nazarewicz, T. Papenbrock, K. A. Wendt, S. Bacca, N. Barnea, B. Carlsson, C. Drischler, K. Hebeler, M. Hjorth-Jensen, M. Miorelli, G. Orlandini, A. Schwenk, and J. Simonis, Neutron and weak-charge distributions of the ^{48}Ca nucleus, Nat. Phys. **12**, 186 (2016).

[26] H. Hergert, S. K. Bogner, T. D. Morris, A. Schwenk, and K. Tsukiyama, The in-medium similarity renormalization group: A novel ab initio method for nuclei, Phys. Rep. **621**, 165 (2016).

[27] G. Hagen, G. R. Jansen, and T. Papenbrock, Structure of ^{78}Ni from First-Principles Computations, Phys. Rev. Lett. **117**, 172501 (2016).

[28] T. D. Morris, J. Simonis, S. R. Stroberg, C. Stumpf, G. Hagen, J. D. Holt, G. R. Jansen, T. Papenbrock, R. Roth, and A. Schwenk, Structure of the Lightest Tin Isotopes, Phys. Rev. Lett. **120**, 152503 (2018).

[29] W. H. Dickhoff and C. Barbieri, Self-consistent green's function method for nuclei and nuclear matter, Prog. Part. Nucl. Phys. **52**, 377 (2004).

[30] P. Navrátil, S. Quaglioni, I. Stetcu, and B. R. Barrett, Recent developments in no-core shell-model calculations, J. Phys. G: Nucl. Part. Phys. **36**, 083101 (2009).

[31] B. R. Barrett, P. Navrátil, and J. P. Vary, Ab initio no core shell model, Prog. Part. Nucl. Phys. **69**, 131 (2013).

[32] D. R. Entem and R. Machleidt, Accurate charge-dependent nucleon-nucleon potential at fourth order of chiral perturbation theory, Phys. Rev. C **68**, 041001 (2003).

[33] A. Nogga, S. K. Bogner, and A. Schwenk, Low-momentum interaction in few-nucleon systems, Phys. Rev. C **70**, 061002 (2004).

[34] K. Hebeler, S. K. Bogner, R. J. Furnstahl, A. Nogga, and A. Schwenk, Improved nuclear matter calculations from chiral low-momentum interactions, Phys. Rev. C **83**, 031301 (2011).

[35] A. Ekström, G. Baardsen, C. Forssén, G. Hagen, M. Hjorth-Jensen, G. R. Jansen, R. Machleidt, W. Nazarewicz, T. Papenbrock, J. Sarich, and S. M. Wild, Optimized Chiral Nucleon-Nucleon Interaction at Next-to-Next-to-Leading Order, Phys. Rev. Lett. **110**, 192502 (2013).

[36] A. Ekström, G. R. Jansen, K. A. Wendt, G. Hagen, T. Papenbrock, B. D. Carlsson, C. Forssén, M. Hjorth-Jensen, P. Navrátil, and W. Nazarewicz, Accurate nuclear radii and binding energies from a chiral interaction, Phys. Rev. C **91**, 051301 (2015).

[37] I. Stetcu, J. Rotureau, B. R. Barrett, and U. van Kolck, An effective field theory approach to two trapped particles, Ann. Phys. **325**, 1644 (2010).

[38] J. Rotureau, I. Stetcu, B. R. Barrett, M. C. Birse, and U. van Kolck, Three and four harmonically trapped particles in an effective-field-theory framework, Phys. Rev. A **82**, 032711 (2010).

[39] S. Tölle, H.-W. Hammer, and B. Ch. Metsch, Universal few-body physics in a harmonic trap, C. R. Phys. **12**, 59 (2011), few body problem.

[40] W. C. Haxton and C.-L. Song, Morphing the Shell Model Into an Effective Theory, Phys. Rev. Lett. **84**, 5484 (2000).

[41] W. C. Haxton, Harmonic-oscillator-based effective theory, in *Opportunities with Exotic Beams* (World Scientific, Singapore, 2007), pp. 117–131.

[42] W. C. Haxton, Form of the effective interaction in harmonic-oscillator-based effective theory, Phys. Rev. C **77**, 034005 (2008).

[43] S. Binder, A. Ekström, G. Hagen, T. Papenbrock, and K. A. Wendt, Effective field theory in the harmonic oscillator basis, Phys. Rev. C **93**, 044332 (2016).

[44] C.-J. Yang, Chiral potential renormalized in harmonic-oscillator space, Phys. Rev. C **94**, 064004 (2016).

[45] E. J. Heller and H. A. Yamani, New L^2 approach to quantum scattering: Theory, Phys. Rev. A **9**, 1201 (1974).

[46] A. M. Shirokov, A. I. Mazur, S. A. Zaytsev, J. P. Vary, and T. A. Weber, Nucleon-nucleon interaction in the j-matrix inverse scattering approach and few-nucleon systems, Phys. Rev. C **70**, 044005 (2004).

[47] D. O. Harris, G. G. Engerholm, and W. D. Gwinn, Calculation of matrix elements for one-dimensional quantum-mechanical problems and the application to anharmonic oscillators, J. Chem. Phys. **43**, 1515 (1965).

[48] A. S. Dickinson and P. R. Certain, Calculation of matrix elements for one-dimensional quantum-mechanical problems, J. Chem. Phys. **49**, 4209 (1968).

[49] J. C. Light, I. P. Hamilton, and J. V. Lill, Generalized discrete variable approximation in quantum mechanics, J. Chem. Phys. **82**, 1400 (1985).

[50] D. Baye and P.-H. Heenen, Generalised meshes for quantum mechanical problems, J. Phys. A: Math. Gen. **19**, 2041 (1986).

[51] D. Lee, Lattice simulations for few- and many-body systems, Prog. Part. Nucl. Phys. **63**, 117 (2009).

[52] S. R. Beane, E. Chang, W. Detmold, H. W. Lin, T. C. Luu, K. Orginos, A. Parreño, M. J. Savage, A. Torok, and A. Walker-Loud (NPLQCD Collaboration), Deuteron and exotic two-body bound states from lattice qcd, Phys. Rev. D **85**, 054511 (2012).

[53] K. Orginos, A. Parreño, M. J. Savage, S. R. Beane, E. Chang, and W. Detmold (NPLQCD Collaboration), Two nucleon systems at $m_\pi \sim 450$ MeV from lattice qcd, Phys. Rev. D **92**, 114512 (2015).

[54] E. Chang, W. Detmold, K. Orginos, A. Parreño, M. J. Savage, B. C. Tiburzi, and S. R. Beane (NPLQCD Collaboration), Magnetic structure of light nuclei from lattice qcd, Phys. Rev. D **92**, 114502 (2015).

[55] N. Ishii, S. Aoki, and T. Hatsuda, Nuclear Force from Lattice QCD, Phys. Rev. Lett. **99**, 022001 (2007).

[56] S. Aoki, T. Hatsuda, and N. Ishii, Theoretical foundation of the nuclear force in qcd and its applications to central and tensor forces in quenched lattice qcd simulations, Prog. Theor. Phys. **123**, 89 (2010).

[57] S. Aoki, T. Doi, T. Hatsuda, Y. Ikeda, T. Inoue, N. Ishii, K. Murano, H. Nemura, and K. Sasaki (HAL Collaboration), Lattice quantum chromodynamical approach to nuclear physics, Prog. Theor. Exp. Phys. **2012**, 01A105 (2012).

[58] T. Inoue, S. Aoki, B. Charron, T. Doi, T. Hatsuda, Y. Ikeda, N. Ishii, K. Murano, H. Nemura, and K. Sasaki (HAL QCD Collaboration), Medium-heavy nuclei from nucleon-nucleon interactions in lattice qcd, Phys. Rev. C **91**, 011001 (2015).

[59] C. McIlroy, C. Barbieri, T. Inoue, T. Doi, and T. Hatsuda, Doubly magic nuclei from Lattice QCD forces at $M\_PS = 469\,\mathrm{MeV/c^2}$, Phys. Rev. C **97**, 021303 (2018).

[60] E. Berkowitz, T. Kurth, A. Nicholson, B. Joó, E. Rinaldi, M. Strother, P. M. Vranas, and A. Walker-Loud, Two-nucleon

higher partial-wave scattering from lattice qcd, Phys. Lett. B **765**, 285 (2017).
[61] T. Yamazaki, Ken-ichi Ishikawa, Y. Kuramashi, and A. Ukawa, Study of quark mass dependence of binding energy for light nuclei in 2 + 1 flavor lattice qcd, Phys. Rev. D **92**, 014501 (2015).
[62] U. V. Kolck, Effective field theory of nuclear forces, Prog. Part. Nucl. Phys. **43**, 337 (1999).
[63] H.-W. Hammer, A. Nogga, and A. Schwenk, *Colloquium*: Three-body forces: From cold atoms to nuclei, Rev. Mod. Phys. **85**, 197 (2013).
[64] D. B. Kaplan, M. J. Savage, and M. B. Wise, A new expansion for nucleon-nucleon interactions, Phys. Lett. B **424**, 390 (1998).
[65] U. van Kolck, Effective field theory of short-range forces, Nucl. Phys. A **645**, 273 (1999).
[66] P. F. Bedaque, H.-W. Hammer, and U. van Kolck, Renormalization of the Three-Body System with Short-Range Interactions, Phys. Rev. Lett. **82**, 463 (1999).
[67] E. Epelbaum, A. Nogga, W. Glöckle, H. Kamada, Ulf.-G. Meißner, and H. Witała, Three-nucleon forces from chiral effective field theory, Phys. Rev. C **66**, 064001 (2002).
[68] P. F. Bedaque, H. W. Hammer, and U. van Kolck, The Three boson system with short range interactions, Nucl. Phys. A **646**, 444 (1999).
[69] C. Ji, D. R. Phillips, and L. Platter, The three-boson system at next-to-leading order in an effective field theory for systems with a large scattering length, Ann. Phys. **327**, 1803 (2012), july 2012 Special Issue.
[70] X. Kong and F. Ravndal, Coulomb effects in low energy proton-proton scattering, Nucl. Phys. A **665**, 137 (2000).
[71] J. Vanasse, D. A. Egolf, J. Kerin, S. König, and R. P. Springer, ^{3}He and *pd* scattering to next-to-leading order in pionless effective field theory, Phys. Rev. C **89**, 064003 (2014).
[72] G. Hagen, T. Papenbrock, D. J. Dean, and M. Hjorth-Jensen, *Ab initio* coupled-cluster approach to nuclear structure with modern nucleon-nucleon interactions, Phys. Rev. C **82**, 034330 (2010).
[73] E. D. Jurgenson, P. Navrátil, and R. J. Furnstahl, Evolving nuclear many-body forces with the similarity renormalization group, Phys. Rev. C **83**, 034301 (2011).
[74] S. A. Coon, M. I. Avetian, M. K. G. Kruse, U. van Kolck, P. Maris, and J. P. Vary, Convergence properties of *ab initio* calculations of light nuclei in a harmonic oscillator basis, Phys. Rev. C **86**, 054002 (2012).
[75] R. J. Furnstahl, G. Hagen, and T. Papenbrock, Corrections to nuclear energies and radii in finite oscillator spaces, Phys. Rev. C **86**, 031301 (2012).
[76] S. N. More, A. Ekström, R. J. Furnstahl, G. Hagen, and T. Papenbrock, Universal properties of infrared oscillator basis extrapolations, Phys. Rev. C **87**, 044326 (2013).
[77] S. König, S. K. Bogner, R. J. Furnstahl, S. N. More, and T. Papenbrock, Ultraviolet extrapolations in finite oscillator bases, Phys. Rev. C **90**, 064007 (2014).
[78] R. J. Furnstahl, G. Hagen, T. Papenbrock, and K. A. Wendt, Infrared extrapolations for atomic nuclei, J. Phys. G **42**, 034032 (2015).
[79] K. A. Wendt, C. Forssén, T. Papenbrock, and D. Sääf, Infrared length scale and extrapolations for the no-core shell model, Phys. Rev. C **91**, 061301 (2015).
[80] M. Lüscher, Volume Dependence of the Energy Spectrum in Massive Quantum Field Theories. 1. Stable Particle States, Commun. Math. Phys. **104**, 177 (1986).
[81] D. Odell, T. Papenbrock, and L. Platter, Infrared extrapolations of quadrupole moments and transitions, Phys. Rev. C **93**, 044331 (2016).
[82] B. Acharya, A. Ekström, D. Odell, T. Papenbrock, and L. Platter, Corrections to nucleon capture cross sections computed in truncated hilbert spaces, Phys. Rev. C **95**, 031301 (2017).
[83] R. G. Littlejohn, M. Cargo, T. Carrington, K. A. Mitchell, and B. Poirier, A general framework for discrete variable representation basis sets, J. Chem. Phys. **116**, 8691 (2002).
[84] J. C. Light and T. Carrington, Discrete-variable representations and their utilization, in *Advances in Chemical Physics*, edited by I. Prigogine and S. A. Rice, Vol. 114 (Wiley-Blackwell, New York, 2007), pp. 263–310.
[85] P. Navrátil, Local three-nucleon interaction from chiral effective field theory, Few-Body Syst. **41**, 117 (2007).
[86] S. König and D. Lee, Volume Dependence of *N*-Body Bound States, Phys. Lett. B **779**, 9 (2018).
[87] C. Forssén, B. D. Carlsson, H. T. Johansson, D. Sääf, A. Bansal, G. Hagen, and T. Papenbrock, Large-scale exact diagonalizations reveal low-momentum scales of nuclei, Phys. Rev. C **97**, 034328 (2018).
[88] R. Machleidt, High-precision, charge-dependent Bonn nucleon-nucleon potential, Phys. Rev. C **63**, 024001 (2001).
[89] J.-W. Chen, G. Rupak, and M. J. Savage, Nucleon-nucleon effective field theory without pions, Nucl. Phys. A **653**, 386 (1999).
[90] E. Epelbaum, H. Krebs, and U.-G. Meißner, Precision Nucleon-Nucleon Potential at Fifth Order in the Chiral Expansion, Phys. Rev. Lett. **115**, 122301 (2015).
[91] P. Navrátil, G. P. Kamuntavičius, and B. R. Barrett, Few-nucleon systems in a translationally invariant harmonic oscillator basis, Phys. Rev. C **61**, 044001 (2000).
[92] R. J. Furnstahl, N. Klco, D. R. Phillips, and S. Wesolowski, Quantifying truncation errors in effective field theory, Phys. Rev. C **92**, 024005 (2015).
[93] Y.-H. Song, R. Lazauskas, and U. van Kolck, Triton binding energy and neutron-deuteron scattering up to next-to-leading order in chiral effective field theory, Phys. Rev. C **96**, 024002 (2017).
[94] S. R. Beane, E. Chang, S. D. Cohen, W. Detmold, P. Junnarkar, H. W. Lin, T. C. Luu, K. Orginos, A. Parreño, M. J. Savage, and A. Walker-Loud (NPLQCD Collaboration), Nucleon-nucleon scattering parameters in the limit of su(3) flavor symmetry, Phys. Rev. C **88**, 024003 (2013).
[95] K. A. Olive and P. D. Group, Review of particle physics, Chin. Phys. C **38**, 090001 (2014).
[96] P. J. Mohr, B. N. Taylor, and D. B. Newell, Codata recommended values of the fundamental physical constants: 2010, Rev. Mod. Phys. **84**, 1527 (2012).
[97] A. H. Wapstra and G. Audi, The 1983 atomic mass evaluation, Nucl. Phys. A **432**, 1 (1985).
[98] O. Dumbrajs, R. Koch, H. Pilkuhn, G. C. Oades, H. Behrens, J. J. de Swart, and P. Kroll, Compilation of coupling constants and low-energy parameters, Nucl. Phys. B **216**, 277 (1983).
[99] H. Kümmel, K. H. Lührmann, and J. G. Zabolitzky, Many-fermion theory in expS-(or coupled cluster) form, Phys. Rep. **36**, 1 (1978).

[100] R. J. Bartlett and M. Musiał, Coupled-cluster theory in quantum chemistry, Rev. Mod. Phys. **79**, 291 (2007).

[101] G. Hagen, T. Papenbrock, D. J. Dean, A. Schwenk, A. Nogga, M. Włoch, and P. Piecuch, Coupled-cluster theory for three-body Hamiltonians, Phys. Rev. C **76**, 034302 (2007).

[102] R. Roth, S. Binder, K. Vobig, A. Calci, J. Langhammer, and P. Navrátil, Medium-Mass Nuclei with Normal-Ordered Chiral $NN+3N$ Interactions, Phys. Rev. Lett. **109**, 052501 (2012).

[103] G. Hagen, T. Papenbrock, and D. J. Dean, Solution of the Center-of-Mass Problem in Nuclear Structure Calculations, Phys. Rev. Lett. **103**, 062503 (2009).

[104] L. H. Thomas, The interaction between a neutron and a proton and the structure of H^3, Phys. Rev. **47**, 903 (1935).

[105] J. A. Tjon, Bound states of ^{4}He with local interactions, Phys. Lett. B **56**, 217 (1975).

[106] E. P. Wigner, Lower limit for the energy derivative of the scattering phase shift, Phys. Rev. **98**, 145 (1955).

[107] I. S. Gradshteyn and I. M. Ryzhik, *Table of Integrals, Series, and Products*, 7th ed. (Elsevier/Academic, Amsterdam, 2007), pp. xlviii+1171, translated from the Russian. Translation edited and with a preface by Alan Jeffrey and Daniel Zwillinger, with one CD-ROM (Windows, Macintosh, and UNIX).

[108] D. R. Phillips and T. D. Cohen, How short is too short? Constraining contact interactions in nucleon-nucleon scattering, Phys. Lett. B **390**, 7 (1997).